US HL-LHC Accelerator Upgrade Project

Analysis of MQXFA07 Test Non-Conformity

Editors: G. Ambrosio, M. Baldini, P. Ferracin

G. Ambrosio, M. Anerella, G. Arnau Izquierdo, M. Baldini, A. Ballerino, C. Barth, A. Ben Yahia, J. Blowers, B. Bulat, D. Cheng, L. Cooley, M. Crouvizier, A. Devred, J. DiMarco, S. Feher, P. Ferracin, L. Garcia Fajardo, S. Izquierdo Bermudez, Elizabeth M. Lee, V. Lombardo, V. Marinozzi, A. Moros, M. Naus, A. Nobrega, I. Pong, S. Prestemon, K. Ray, G. Sabbi, J. Schmalzle, S. Sgobba, E. Todesco, M. Turenne, G. Vallone, M. Yu, X. Wang

TABLE OF CONTENTS

1. Introduction

MQXFA07 is the 5th and last MQXFA pre-series magnet fabricated by AUP. Main data about components and assembly of this magnet can be found in the MQXFA07 Fabrication report [1].
MQXFA07 did not meet MQXFA acceptance requirements [2] during vertical test [3]. This report presents the analysis of MQXFA07 components possibly related to the limited test performance.

2. Test Results and Analysis

2.1. Quench History

MQXFA07 Quench history plot is shown in Fig 2.1 and was presented at the MQXFA07 Test Results Meeting [3]. Figure 2.1 shows that MQXFA07 started training above 15 kA and reached 16.1 kA in 3 quenches. Subsequently it showed a detraining of 800 A between quench #4 and quench #5. Quenches #7-#9 and quench #13 (all of them at 1.9 K and with 20 A/s ramp rate) have quench current in the range 15 – 15.1 kA, showing a drop of about 1 kA with respect to the quench current reached in quenches #3 and #4.
Figure 2.1 shows that all limiting quenches started in a single coil (Coil 214) and in the same voltage-tap segment (A3-A4). It also shows:

- reverse temperature dependence (higher quench current at 4.5 K than at 1.9 K, with standard 20 A/s ramp rate), with about 800 A increase at 4.5 K
- and reverse ramp-rate dependence (higher quench current at ramp rate higher than 20 A/s, at 1.9 K) with 1486 A and 1332 A increase at 100 and 60 A/s respectively, using the last quench at 20 A/s as reference.

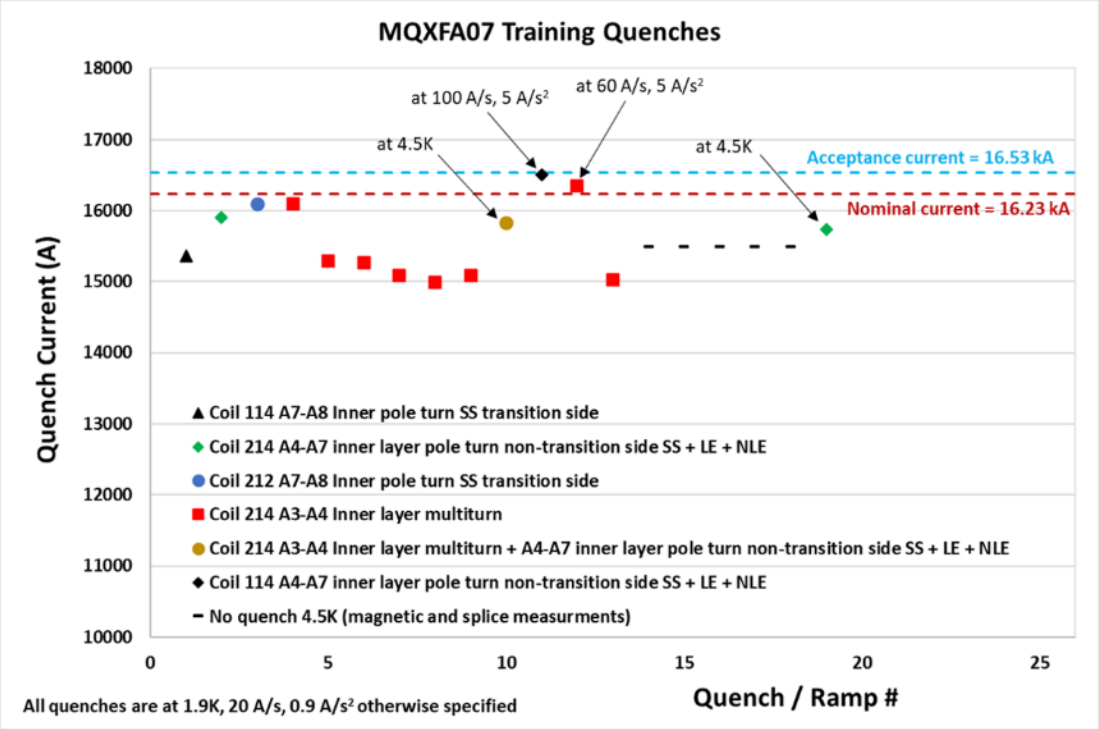

Figure 2.1: MQXFA07 quench history

2.2. Limiting quenches in Coil 214

All limiting quenches in coil 214 started within segmented A3-A4 on the inner layer. As shown in Fig. 2.2, this is a multiturn segment including turns 2 to 6 counting from the pole. Turns 2-5 are included in the pole-block multiturn, whereas turn 6 is the first turn outside the wedge.

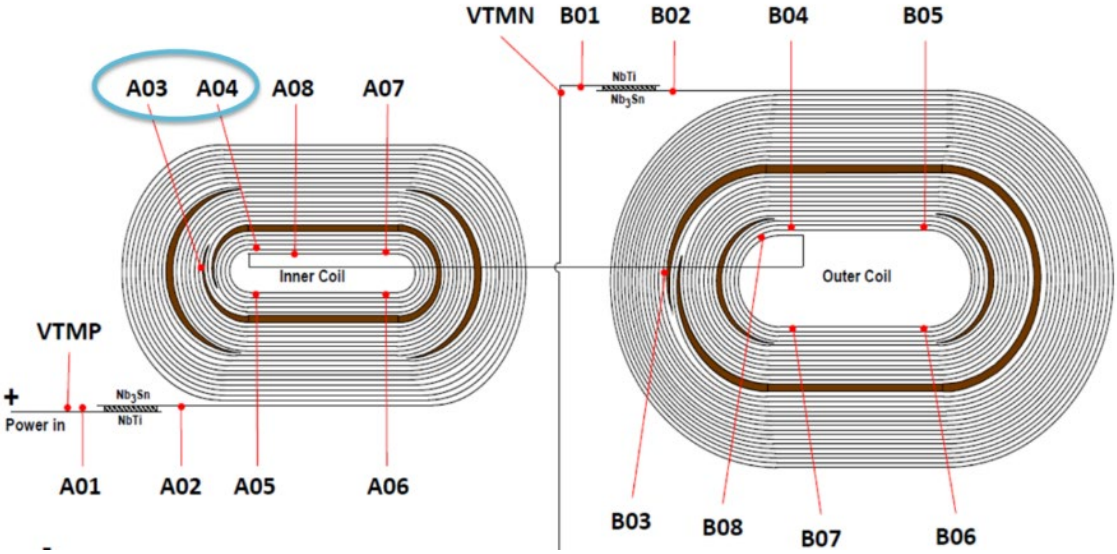

Figure 2.2: Voltage taps in MQXFA pre-series coils. All limiting quenches in coil 214 started with the multi-turn segment A03-A04.

2.3. Quench antenna data

A quench antenna with full length Z-coverage was used during the magnet test. It is made of 111 50 mm-long flex circuits. Theta detection was achieved using 12 full length Dipole and quadrupole buck radial circuits.

In Fig. 2.3, all quench positions along Z-axis observed during the magnet training are displayed. All limiting quenches in coil 214 (Q3), observed at 1.9 K and 20 A/s, take place in the same longitudinal position along the coil, at around 2000 mm. This location corresponds to the beginning of the lead end of the coil.

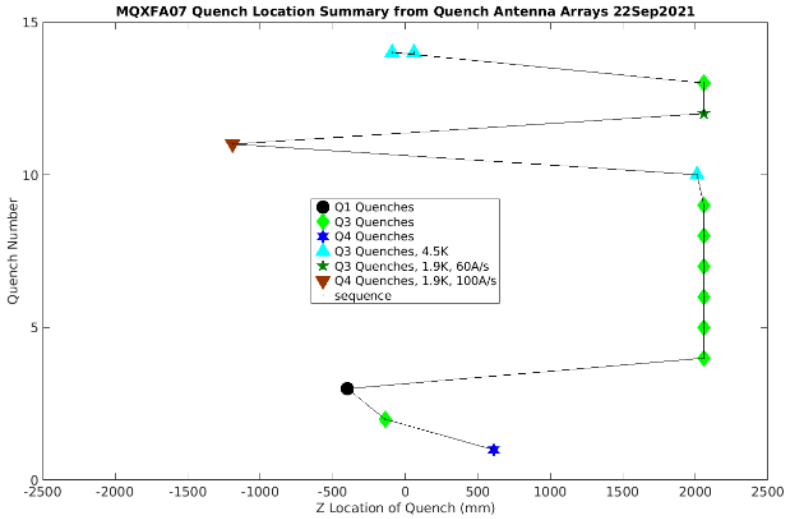

Figure 2.3: Signals of the quench antenna and localization along the coil axis for quench 9 (1.9 K, 20 A/s)

Figure 2.4 shows quench antenna signals (of quench #9) overlapped to a coil drawing. The quench starts at about -23 ms (from quench detection) at the longitudinal position where the turns of the pole-block go around the pole tip. The raw data are shown in Fig. 2.5 for quench 9. The contribution of the last 10 channels of the antenna is displayed. The quench start is detected by channel 95.

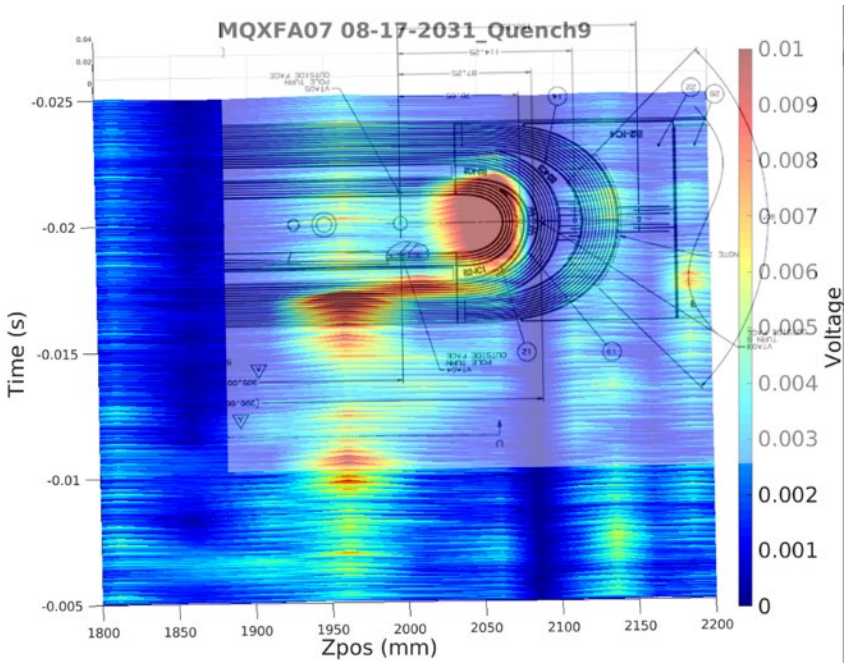

Figure 2.4: Signals of the quench antenna and localization along the coil axis for quench 9 (1.9 K, 20 A/s)

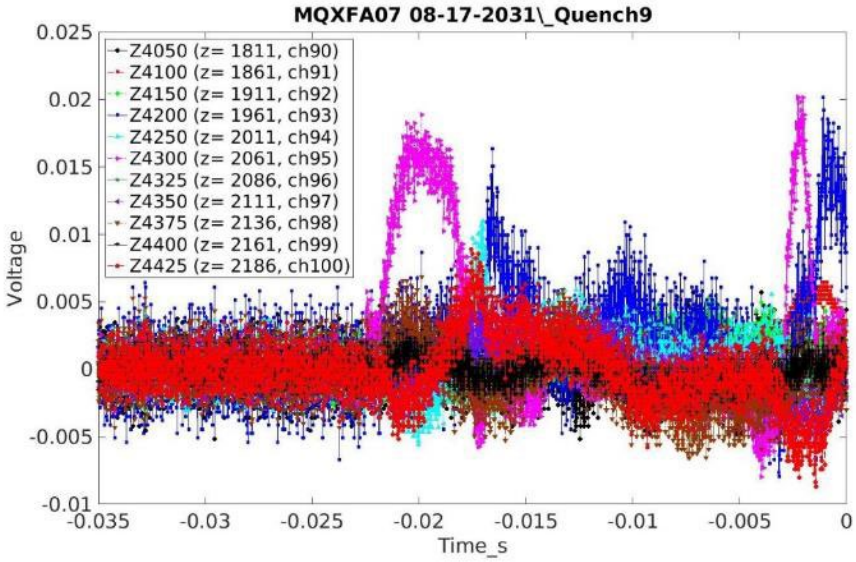

Figure 2.5: Signals of the quench antenna from channel 90 to 100 for quench 9 (1.9 K, 20 A/s)

2.4. Strain Gauge data analysis

According to the strain gauge measurements taken during magnet fabrication, the coils, shells and rods were pre-loaded consistently to the target values (see Fig. 2.6 left), and the coil peak stress during bladder operation was mantained within the -110 MPa set as a limits in the magnet pre-load specifications (see Fig. 2.6 right). During test, and in particular during excitation the coil exhibited the usual unloading, indicating that the coil pre-load after cool-down was consistent with previous magnets (see Fig 2.7).

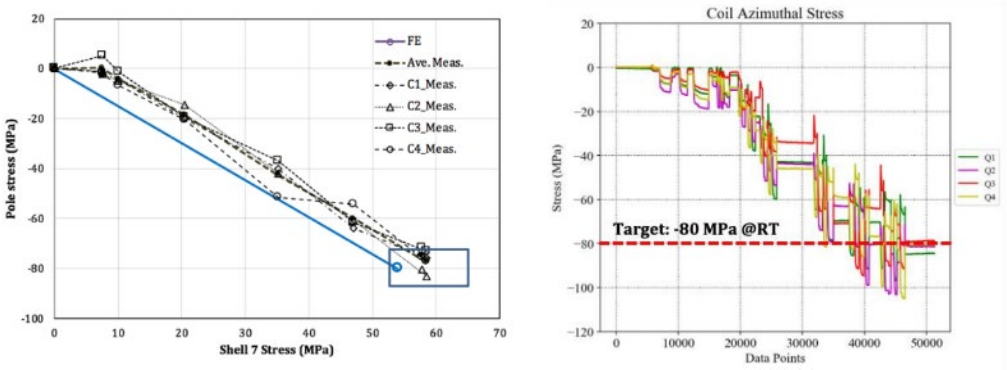

Figure 2.6: Left: coil pole vs shell stress during magnet pre-loading (the square indicates the acceptable target values). Right: details of the coil pole stress during bladder operation, with peak stress <110 MPa.

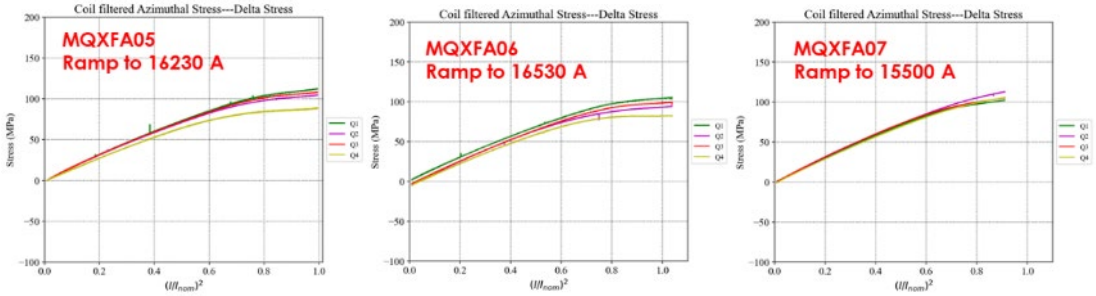

Figure 2.7: Coil pole unloading during powering in magnet A05, A06 and A07.

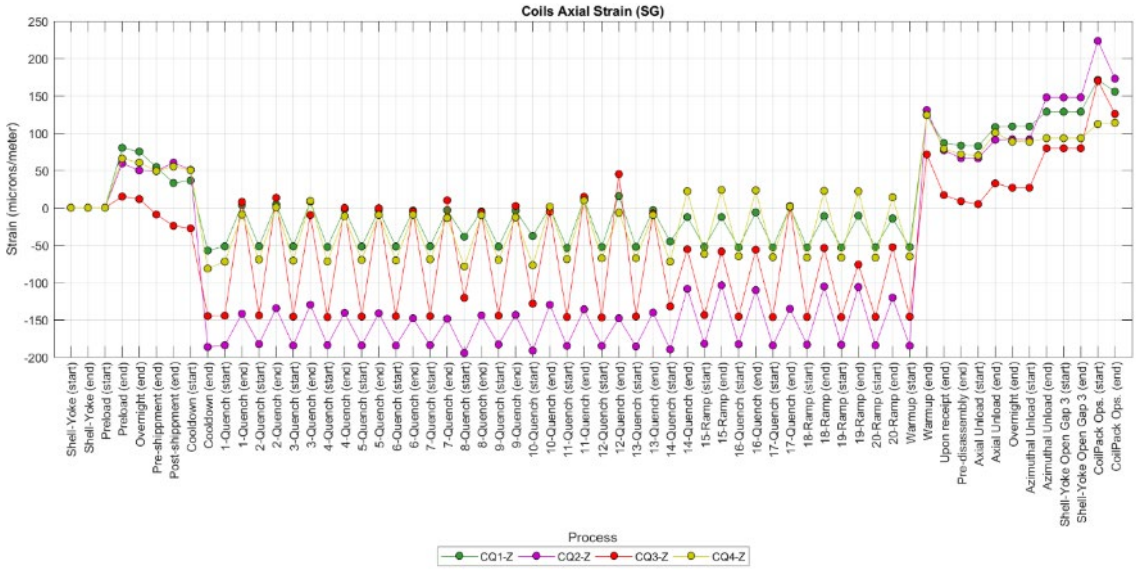

Figure 2.8: Coil axial strain history.

The analysis of the strain gauges was focused in particular on the mechanical behavior of coil Q3 (the limiting coil). The most relevant difference with respect to the other coils was related to coil pole axial strain. As can be seen in Fig. 2.8, where the whole magnet history is plotted, coil Q3 exhibited a lower axial strain at the end of the room temperature pre-loading, and a larger axial strain variation during magnet powering. An analysis of this behavior by mean of finite element simulations is described in chapter 5.

2.5. Effect of assembly and test on field quality

Indico page: https://indico.fnal.gov/event/51196/
Indico page: https://indico.fnal.gov/event/53337/

The analysis of the magnetic measurements of A07 (full cycle of assembly test and disassembly) pointed out that

- In terms of coil deformations during assembly cold test and disassembly:
  - The behaviour is consistent to other magnets
  - The coils radial deformation before/after cold test estimated by the magnetic measurements is consistent with mechanical measurement of coil pack (-0.13 mm vs. [-0.10,-0.15]) but an additional reduction of the coil arc length by 0.12 mm is required to fit both T.F. and b6 (b10)
  - Similar, but 2x larger effect, is seen from coil pack to assembled magnet
  - Assembly effect is largely reversible at disassembly while cold test causes permanent changes (see Fig. 2.9)
- In terms mechanical deformations from ANSYS (see Fig. 2.10)
  - Magnitude of calculated changes in non-allowed harmonics are roughly of the same order as found in BNL measurements from warm to nominal; however, A07/A08 measurements show different changes despite similar pole key gaps.

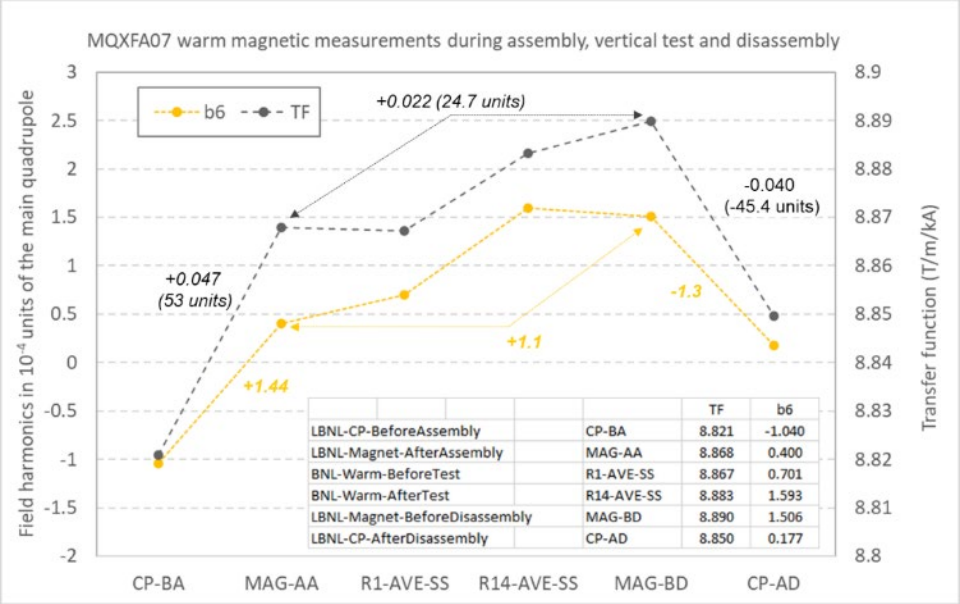

		TF	b6
LBNL-CP-BeforeAssembly	CP-BA	8.821	-1.040
LBNL-Magnet-AfterAssembly	MAG-AA	8.868	0.400
BNL-Warm-BeforeTest	R1-AVE-SS	8.867	0.701
BNL-Warm-AfterTest	R14-AVE-SS	8.883	1.593
LBNL-Magnet-BeforeDisassembly	MAG-BD	8.890	1.506
LBNL-CP-AfterDisassembly	CP-AD	8.850	0.177

Figure 2.9: Variation of b6 and TF during assembly, test and disassembly.

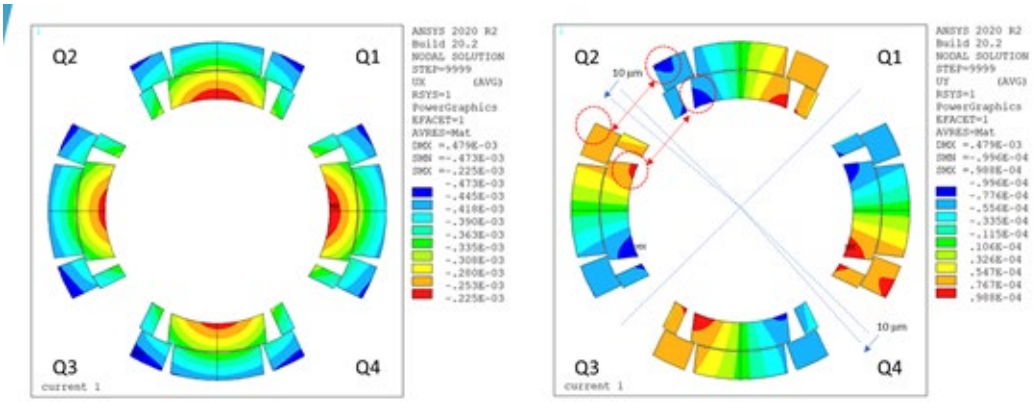

Figure 2.10: Mechanical deformations computed by ANSYS.

2.6. Limiting quench mechanism

The reverse temperature and ramp-rate dependences (Fig 2.1), described in Section 2, are clear signatures of the mechanism understood as cause of MQXFA07 limited performance: **self-field instability enhanced by conductor damage**. This mechanism is caused by some conductor damage that pushes more current in a few strands (or in the not-damaged section of a few strands) triggering the self-field instability in those strands. This mechanism was found in a LARP Long Quadrupole [4], although in that magnet the damage was likely in a low field area, therefore triggering thermo-mechanical instability with its typical flux jumps.

More recently, MQXFS3a short model [5] had a quench history (Fig 2.11) very similar to MQXFA07 with reverse temperature dependence, reverse ramp-rate dependences, quenches around 15 kA at 19.K and 20 A/s, and quench start location in the pole block of the lead end of the limiting coil.

In the pole block segment (A3-A4) where MQXFA07 limiting quenches started, the magnetic field ranges between 5.2 T (minimum on turn 6) and 9.4 T (maximum on turn 2) at 15.3 kA. This magnetic field intensity is consistent with the magnetic field minimum observed for self-field instability [6 – 7] in RRP conductors similar to the MQXF conductor.

The performance drop after quench #4 shows that the conductor damage triggering the self-field instability occurred or was exacerbated during current ramp or quench #4. It may have started during quench #3 because the quench location moved to the limiting zone from quench #3 to quench #4.

Measurements of MQXFA strand stability were performed at CERN and are reported in Appendix 1. Measurements were done on strands extracted from left-over sections of the cables used for coil 214 and 213 (limiting coils in MQXFA07 and MQXFA08, respectively). All samples tested were stable up to 2 kA at both 1.9 and 4.3 K. Therefore, the conductor damage triggering MQXFA07 instability is expected to have involved several strands. It is also possible that the mechanical damage may have caused both reversible and irreversible degradation putting some strands in a condition quite different from that of a typical stability measurement.

Since analysis of voltage taps and quench antenna data was able to locate the start of the limiting quenches in the lead end of coil 214, an inspection plan was developed for this coil. Details and outcome are presented in section 6 of this document.

During the vertical test of MQXFA08, the magnet tested at BNL Vertical Test facility after MQXFA07, it was found that the splice between the magnet negative lead and the test facility had resistance equal to 42 nohm at the time when this splice was measured [8]. It was also found that the resistance of this splice had not been measured during MQXFA07 vertical test. The magnet negative lead is connected to the inner layer of the coil in Quadrant 3. Coil 214, MQXFA07 limiting coil, was in quadrant 3 and limiting quenches started in the Inner Layer Lead End (i.e. close to the point where coil 214 was connected to the magnet negative lead). Analysis of the possible impact on magnet performance of high resistance in the splice between the magnet negative lead and the test facility will be presented in [8].

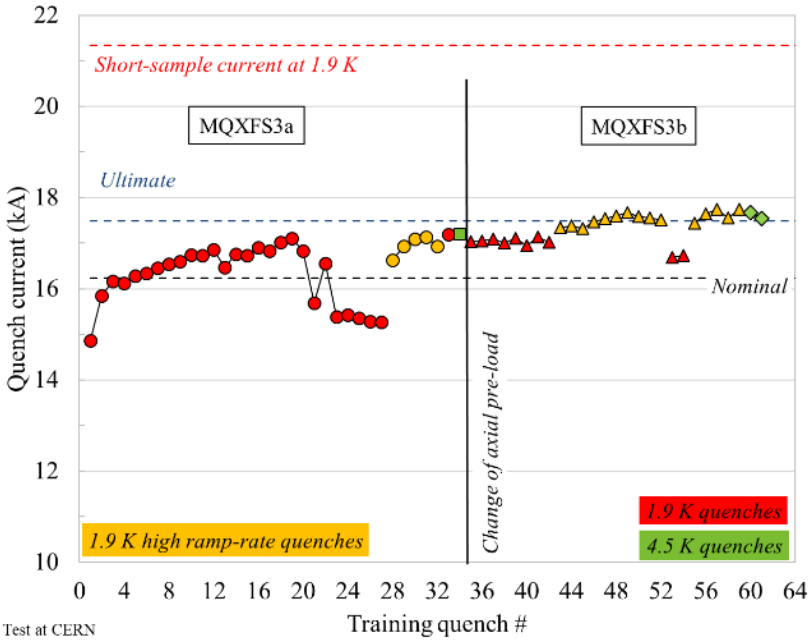

Figure 2.11: Quench history of MQXFS3 in its original assembly (3a) and after change of axial pre-load (3b).

3. Coil fabrication and magnet assembly

3.1. Coil 214 Fabrication

Coil 214 is an MQXFA Pre-Series coil fabricated at BNL. The main features of the conductor used in this coil, and its main fabrication parameters are presented in MQXFA07 Fabrication Report [1]. It should be noted that the fabrication of this coil was affected by the COVID-19 lockdown. The inner layer had been wound and cured when BNL had to go in lockdown. The coil was secured to the winding mandrel with VELCRO straps and pushers bolted in place. It remained in this condition for 14 weeks before work was resumed by winding the outer layer. Figure 3.1 shows coil 214 as it was setup for the lab shutdown. The fabrication of six other MQXFA coils (3 at BNL and 3 at FNAL) was interrupted by the lockdown. Table I shows for these coils the status during lockdown, idles time, and outcome of vertical test if already performed.

Usually the outer layer of a coil is wound and cured a few days after the inner layer. Subsequently, the tensioners keeping the coil stretched are removed. During the 14 weeks when coil-214 inner-layer was in storage with tensioners on, the bonding between wedges and end-spacers may have degraded.

Table 1: MQXFA coils whose fabrication was interrupted by COVID-19 lockdown. Test status is green if magnet met requirements during vertical test; it is red if it did not meet requirements.

Coil #	Idle time	Status during lockdown	Test status
122	~9 weeks	OL impregnation prep, no lead soldering.	Tested in MQXFA06
123	11 weeks	Reaction was stopped during first ramp at 76 C. Coil in reaction fixture inside oven.	Tested in MQXFA06
124	8 weeks	Coil winding prep mostly complete. 1st turn not wound.	Tested in MQXFA07, will be used in MQXFA07b
211	~14 weeks	Impregnated coil. Coil remained closed in the impregnation fixture, hanging in the impregnation tank.	Tested in MQXFA06
212	~14 weeks	Reacted coil with leads soldered. Coil stored in the lower half of the reaction fixture, clamped with several formblocks and covered in plastic.	Tested in MQXFA07, will be used in MQXFA07b
213	~14 weeks	Reacted coil. Coil remained closed in the reaction fixture, in the oven.	In MQXFA08
214	~14 weeks	Inner layer wound and cured. Coil stored on mandrel in winding machine, inner layer pushers bolted in place supporting midplane, numerous Velcro straps securing coil OD and coil ends, coil covered in plastic.	Limiting coil in MQXFA07

Figure 3.1: coil 214 as it was setup for the lab shutdown

3.2. Discrepancy Reports during Coil 214 Fabrication

Two Discrepancy reports were generated during fabrication of coil 214. They are listed below, followed by comments about possible relevance to the MQXFA limitation.

DR AM-164 describes that "during winding of layer 1, approaching turn 6, the cable collapsed". The cable was repaired following standard practice (see details in Fig 3.2), and winding was resumed. "The next morning it was noted that some strands were out of position at the lead end."

Later on the L3 for coil fabrication at BNL added that when in the morning the team noticed the strands a bit out of place, they unwound the half-turn to put the strands back in position, apply binder and cure with a heat gun, before continuing winding.

The position of the conductor affected by this DR is shown in yellow color in Figure 3.3. Voltage tap A03 is set on the outside of the first lead-end spacer on turn 6. Therefore, the conductor affected by this DR is within voltage tap pair A3-A4, that is the quenching segment in the MQXFA07 limiting quenches. It is also possible that during the long interval between the curing of coil-214 inner layer and its epoxy impregnation a strand may have moved out of place.

After MQXFA07 dis-assembly, tomography of both ends of coil 214 was performed in order to assess if there is any strand out of place. Results are shown in section 6.2.

MAGNET DISREPANCY REPORT

DR NUMBER: AM-164

Preliminary: 3-16-20
Action Required: 3-16-20
Final: 3-3-20

Part No: F10030927 Rev		Traveler No.: AUP-110	Rev:
Part Name: Coil Winding		Traveler OP No.: 820	
Qty: 1	Ser. No./Lot No.: QXFA214	Operation: Winding Layer 1	
Initiator: W. Themann	Life No.: 18656	Date: 3-11-20	
Type of Problem: (Check) Mechanical ✓	Electrical	Other	

Description (Continue on reverse side if required)	Disposition (RWK, RPR, UAI, SCP)	CE	DQAR
During winding of layer 1, approaching turn 6, the cable collapsed. Winding was paused, tension reduced, strands were worked back into position, binder applied and winding resumed. Another 1/2 turn was wound and winding was paused for the night. The next morning it was noted that some strands were out of position at the lead end.	RWK		

Instructions: Continue on additional sheets if required	Name	Life #	Date
Pause winding, unwind 1/2 turn, reduce cable tension, use hands / duckbill pliers to work strands back into position, apply binder to cable and cure with heat gun, increase cable tension and wind in manual mode back to NL end, resume winding in automatic mode.		15764	3/10/20

Figure 3.2: Snapshot of DR AM-164 Description and Instructions.

Coil 214 – collapsed cable location

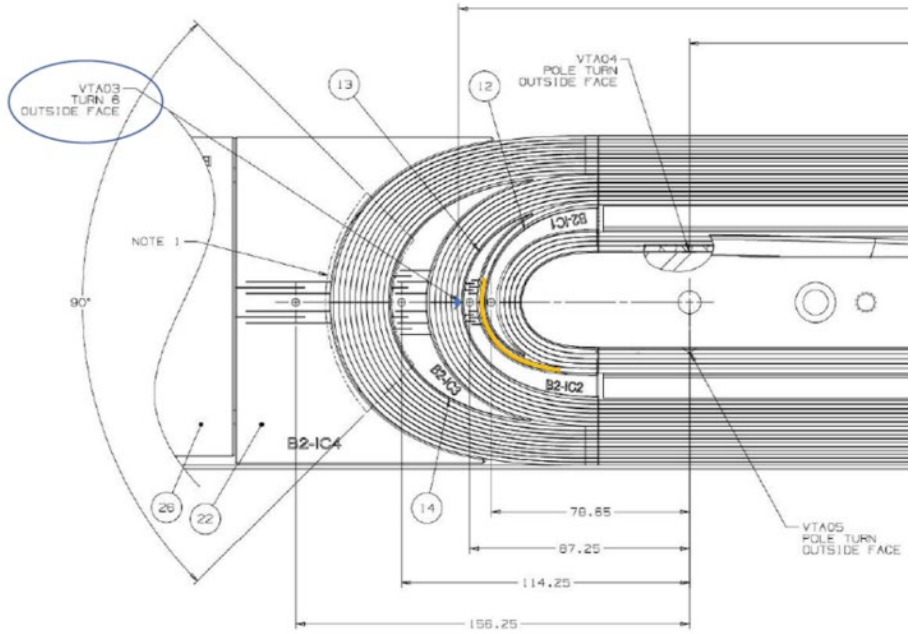

Figure 3.3: Inner layer coil drawing showing in yellow the position of coil-214 cable affected by DR AM-164

DR AM-185 reports that during preparation for epoxy-impregnation the saddles at both coil ends had areas where ceramic coating had chipped away at the tip where saddle contacts the coil. Kapton and fresh fiberglass ribbon were inserted to cover these areas.

Saddles are in contact with the coil midplane turns (on inner and outer layers), which are included in multiturn blocks A02-A03 and B02-B03. These segments do not show voltage rise in any quench, and there is no sign of any electrical issue. Therefore, this discrepancy does not appear related with the magnet limiting mechanism.

Detailed information about all the coils used in MQXFA07 (114, 124, 212, 214) are found in the MQXFA07 fabrication report (docdb-4293).

3.3. Investigation of coil 214 Quality

An extensive investigation of coil 214 quality was done and is reported in [9]. The investigation covered also coil 213 that limited MQXFA08 magnet. The focus of this investigation was looking at the travelers, discrepancies, components, and quantitative data associated with the coils and magnets, to see if any asymmetries can be identified that would indicate any differences between the two coils, or their location in the magnets, and all the other coils or quadrants.

The conclusion of this investigation was: *"No substantive differences have been identified between the two coils, or location in the magnet, and the rest of the BNL coils or magnet quadrants. With a small number of exceptions, all differences fall within normal statistical variation. Regarding the exceptions, we were unable to think of any ways in which they would affect the coil's performance in the manner observed"*.

3.4. Magnet assembly, preload and NCRs

MQXFA07 assembly is described in MQXFA07 fabrication report (US-HiLumi-doc-4197).

There was one Off-normal working procedure after magnet preloading. This is described by NCR-220. Following preloading, it was noted that the RE axial end plate on MQXFA07 was off-center (shifted down and to the left); to correct this issue, the magnet needed to be unloaded and realigned. The off normal work procedure is documented in docDB-4210 and MQXFA-NCR-0220 and is similar to work done on MQXFA06 NCR-164. The following corrective actions were taken:

1. Unload ~50% of the load (to ~470 με)
2. Check strain gauges to verify repeatability
3. If numbers are proper, reduce force to light contact (~50 με) to maintain friction
4. Move RE endplate using bracket tooling and align (same tooling as used on MQXFA06)
5. Reload to 950 με rod strain
6. SG readings maintained throughout process
7. Verify SG readings are ok

Figures 3.4 through 3.6 show the stress/strain reading before/during/after the off-normal work procedure. The coil axial strain and azimuthal stress as well as the rod strain were maintained after the work was completed.

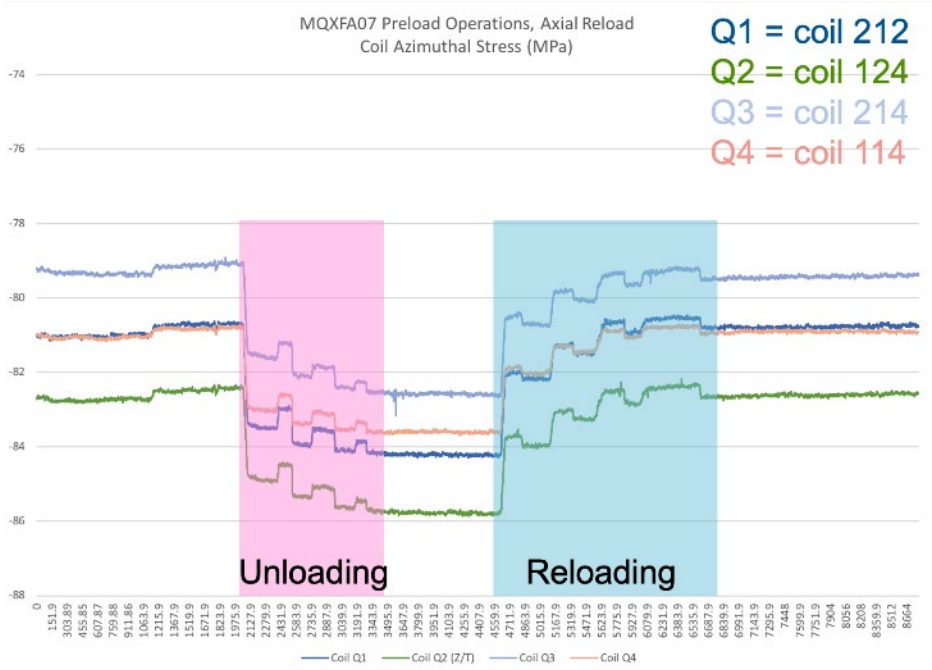

Figure 3.4: Coil azimuthal stress during off-normal work procedure for MQXFA07 NCR-220

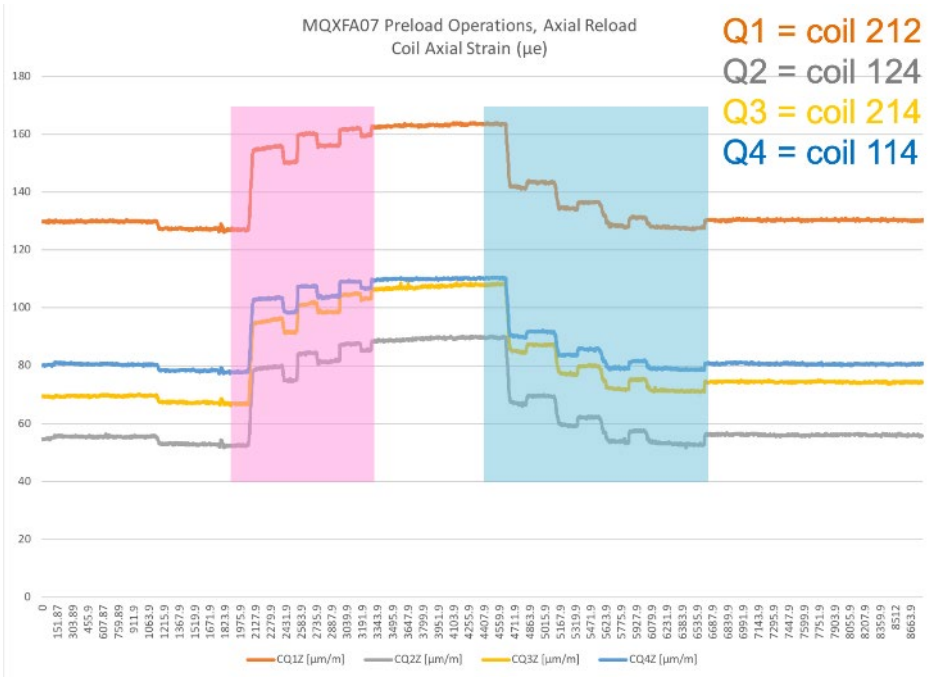

Figure 3.5: Coil axial strain during off-normal work procedure for MQXFA07 NCR-220

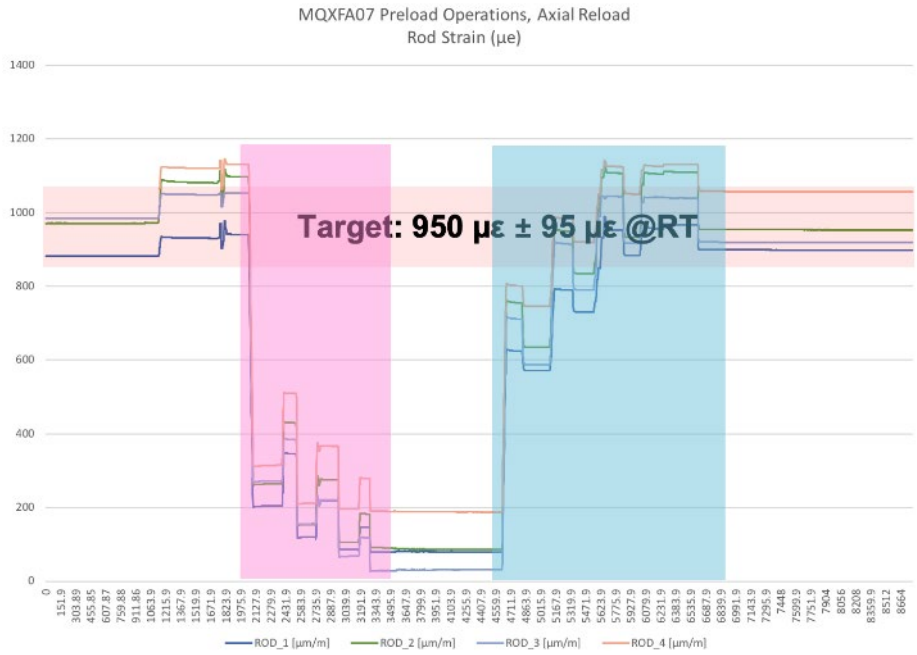

Figure 3.6: Rod strain during off-normal work procedure for MQXFA07 NCR-220

3.5. Covid impact on magnet assembly

Two off-normal working conditions, related to the regulations implemented at LBNL to address the COVID pandemic, affected the coil-pack assembly of magnet MQXFA07. To clarify these modifications, we provide a representation of the coil-pack assembly in Fig. 3.7 (top), with on the left a cross-section of the coil-pack assembly, and on the right a 3D side view of coil-pack assembly along the longitudinal direction. The *left* and *right* side of the cross-section, and the *lead-end*, *center*, and *return-end* in longitudinal view are also indicated. The changes are:

1. From MQXFA05 (the first magnet assembled after the LBNL Covid shut-down) up to magnet MQXFA09, the following change in the coil-pack assembly procedure was implemented:
    a. In the original procedure, which was followed before the Covid shut-down (i.e. before up to magnet MQXFA04), the bolting of the pads around the collared coil was executed in the following way (see Fig. 3.7, bottom left):
        i. two technicians were starting bolting the pads from the longitudinal center of the coil-pack, being one technician on the left side and the other on the right side;
        ii. after bolting the central pads, the two technicians were bolting the adjacent pads alternatively towards the lead end and towards the return end;
        iii. in this process, the two technicians were moving in a simultaneous way, and were therefore always facing each other.
    b. In the procedure adopted after the LBNL Covid shutdown (i.e. from MQXFA05 to MQXFA09) the two technicians were still starting the bolting procedure from the central pads, but they were then moving in opposite directions, still alternating the steps towards the lead and return end (see Fig. 3.7, bottom right). The purpose of this change was to minimize the time when the technicians were in close proximity (i.e. facing each other).

2. Starting from magnet MQXFA06, a change of personnel working on the coil-pack assembly was executed. Specifically, the technician who had been leading the coil-pack assembly operations up to magnet MQXFA05 was removed from the task. In fact, according to the regulations adopted by LBNL to address the Covid pandemic, assembly processes requiring personnel to work in close proximity had to be carried only by vaccinated technicians (protocol A). As a result, the lead technician for the coil-pack assembly, who was not vaccinated (protocol B), was assigned to task which did not require working close to other personnel. The aforementioned technician was then reassigned to the coil-pack assembly starting from magnet MQXFA10 (reassembly) and he played a key role in defining the new coil pack-assembly procedure aimed at minimizing the difference in pole key gap among the four quadrants.

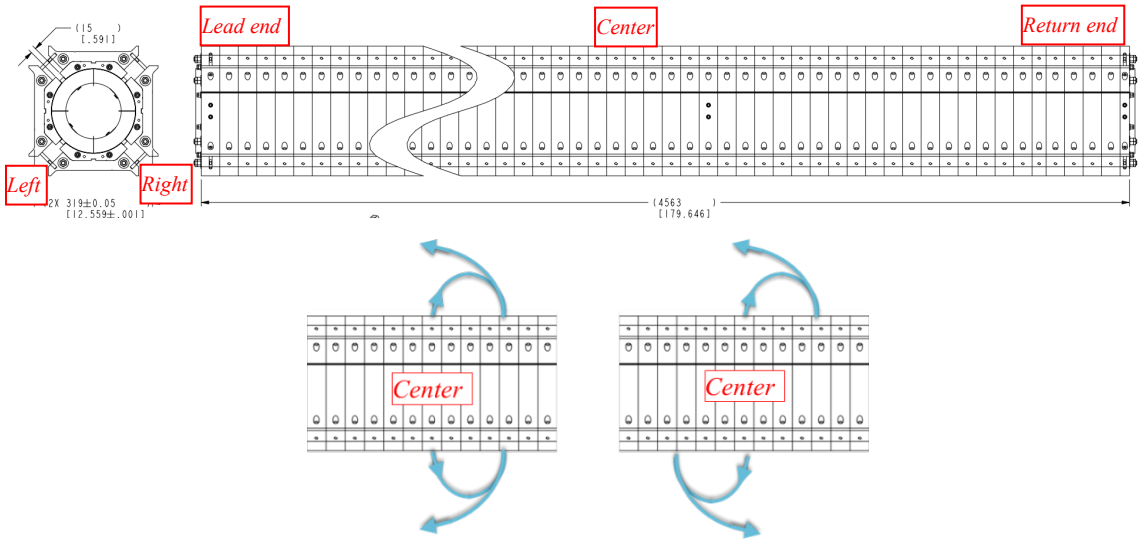

Figure 3.7: Coil pack sub-assemblies: on top, cross-section (left) and full 3D view (right) with the series of bolted pads around coil and collars. Bottom: sequence of bolting before (left) and after (right) change #1.

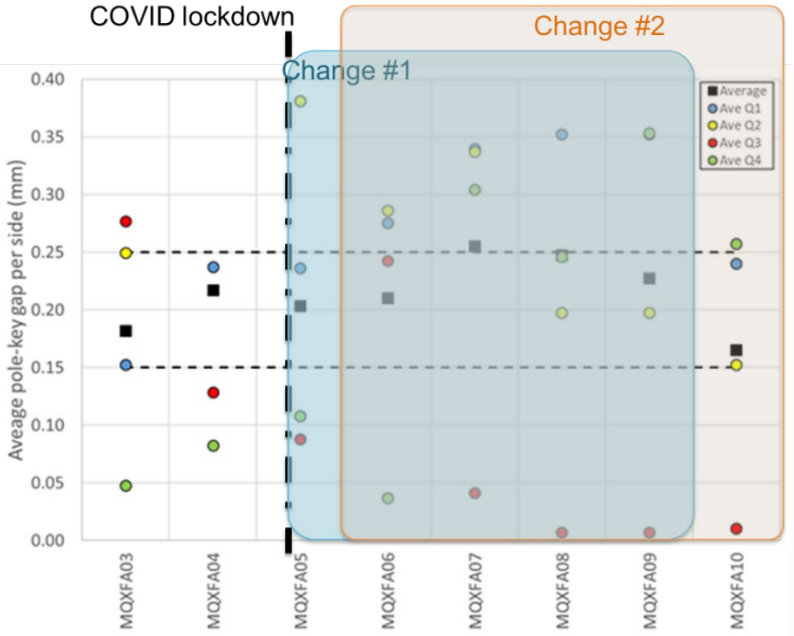

Figure 3.8: Average pole-key gaps (per key side) in magnets MQXFA03 to MQXFA10.

Figure 3.8 shows the average pole-key gap in each quadrant and for each magnet from MQXFA03 to MQXFA10. It can be noted that the minimum pole-key gap had a positive trend in magnets MQXFA03-MQXFA05, whereas it showed a negative trend starting with MQXFA06 (i.e. when change #2 was implemented). Therefore, it is our understanding that the changes due to Covid requirements contributed to small pole-key gaps in quadrant 3 of MQXFA07 and MQXFA08, which did not meet test requirements. Magnets MQXFA09 and MQXFA10 were disassembled before test, and MQXFA10 met test requirements after it was re-assembled with uniform pole-key gaps.

4. Magnet dis-assembly and inspection

After the test at BNL and the shipment to LBNL, the magnet was inspected and disassembled following the plan described in "MQXFA07 Inspection Plan" (US-HiLumi-doc-4222). The most relevant conclusions of the measurements taken during the disassembly are described in the following sub-sections.

4.1. Coil-pack dimensions

After unloading and disassembly, the coil-pack dimensions were measured and compared with the values taken during the first assembly (before the test). From A07 (before the test) to A07p (after the test) the coil-pack reduced in size by 0.2 to 0.3 mm (see Fig. 4.1).

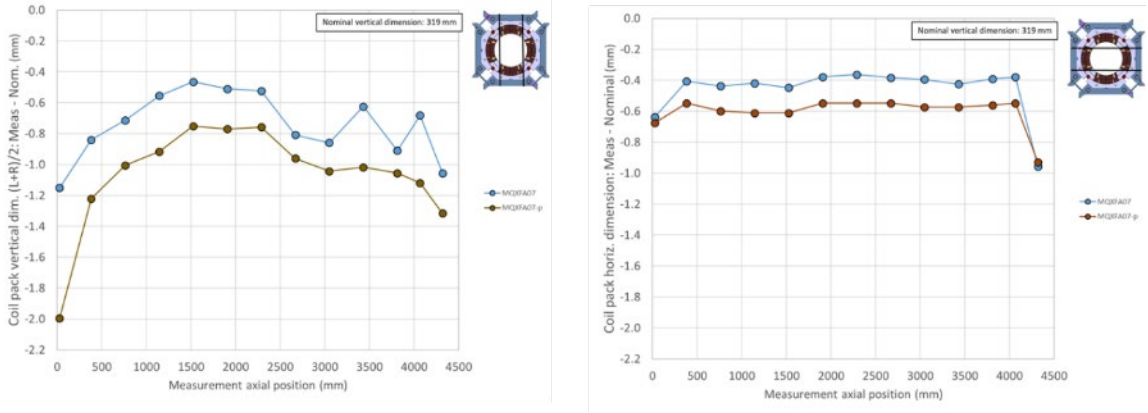

Figure 4.1: Coil-pack dimensional measurements before the test (A07) and after the test (A07p).

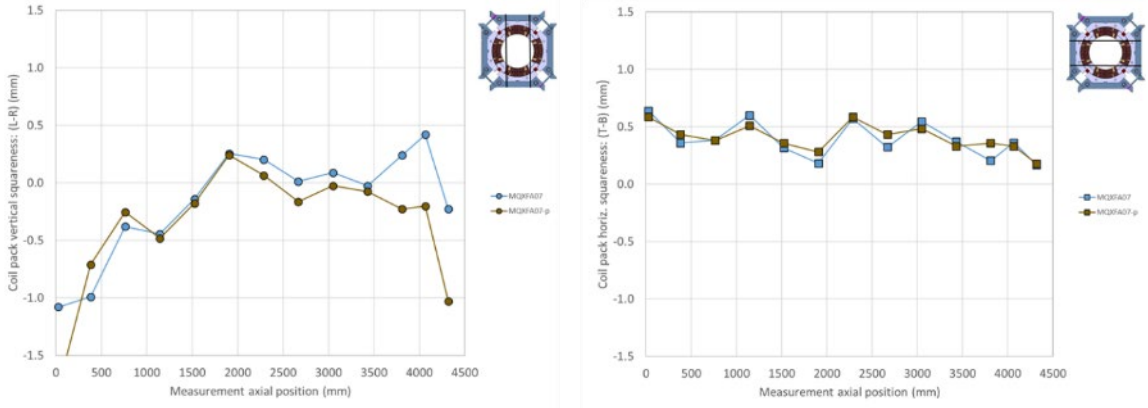

Figure 4.2: Coil-pack squareness measurements before the test (A07) and after the test (A07p).

This variation corresponds to a change in coil outer radius of -0.100 to 0.150 mm, or a change in coil arc length of -0.150 to -0.235 mm. The coil-pack size profile did not change, and maintained a significant size reduction in correspondence of the magnets ends. Also, the squareness measurements indicated that the coil pack did not change from before to after the test (see Fig. 4.2), and kept a trapezoidal shape, shown by the difference between the top (T) and bottom (B) horizontal measurement (Fig. 4.2 right).

The reduction of size in coil pack shown in Fig. 4.1 can be partially explained with the reduction in coil arc length which was measured by CMM data taken on the coils after the test. Specifically, the mid-plane average variation with respect the nominal variation changed from before the test (A07) to after the test (A07p) as follows:

- Coil 124: -0.071 to -0.105
  - Δ = -0.034 mm per mid-plane = -0.068 mm in arc length
- Coil 212: -0.023 to -0.055
  - Δ = -0.032 mm per mid-plane = -0.064 mm in arc length
- Coil 114: -0.083 to -0.130
  - Δ = -0.047 mm per mid-plane = -0.094 mm in arc length
- Coil 214: -0.034 to -0.055
  - Δ = -0.021 mm per mid-plane = -0.042 mm in arc length

4.2. Pole key gap

Consistently with the trapezoidal shape of the coil pack, a non-uniformity in the distribution of the pole key gaps was observed, both before and after the test. In Fig. 4.3, the pole key gap measurements in each quadrant as a function of the axial position, before the test (A07) and after the test (A07p), are shown. The specifications for the pole gaps, indicated by the dashed lines in the figures, state that the average pole key gap (per side) among the four coils on each longitudinal location shall be +0.200 ±0.050 mm. It can be seen that the average among 4 quadrants is on spec, both before and after the test, but a significant variation among quadrants is present. In particular, in Q3 an extremely low gap is observed before the test, and it becomes null after the test. The measurements before and after the test show that the gaps decreased by about 0.100 mm, but the same profiles among the quadrant is maintained, demonstrating the neither the room temperature loading, nor the cool-down or the test, corrected the non-uniformities in the pole key gaps.

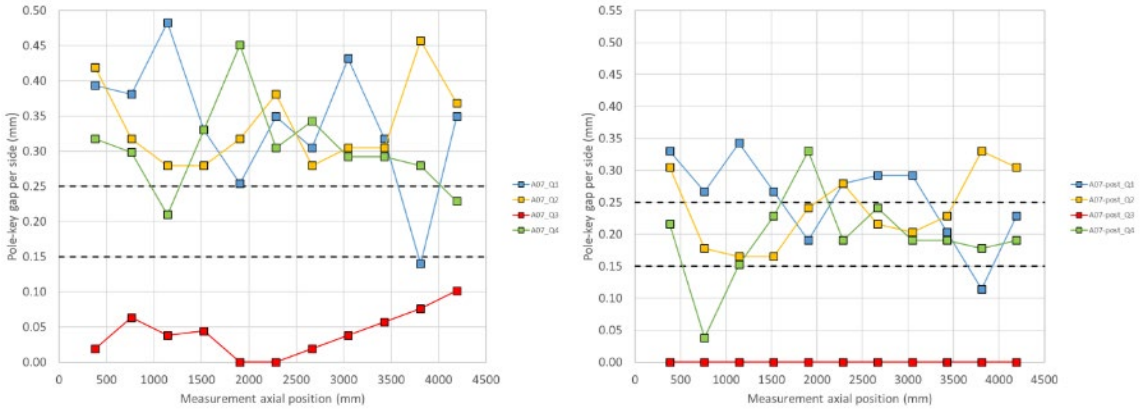

Figure 4.3: Pole key gap measurements in each quadrant as a function of the axial position, before the test (A07) and after the test (A07p). The dashed lines indicate the spec values of the average of among the four quadrants on each longitudinal location.

4.3. Visual observations after coil-pack disassembly

After the coil pack-disassembly, coils, ground isolation layers and pole keys were inspected. In quadrant 3, deep imprints in the Kapton indicating collar lamination lines, G11 grain, and "lower pressure" spots at every hole in the G11 keys (Fig. 4.4). These imprints, all indicative of a higher pressure, were not seen in the other quadrants. In addition, the G11 keys in Q3 also showed high pressure "imprints" of collar lamination gaps (Fig. 4.5), not observed in the other quadrants.

The coil inner surface was characterized by many bubbles/blisters, predominantly on the LE (Fig. 4.6 and 4.7). More observations and comments may be found at section 6.1 "Coil 214 Visual Inspection".

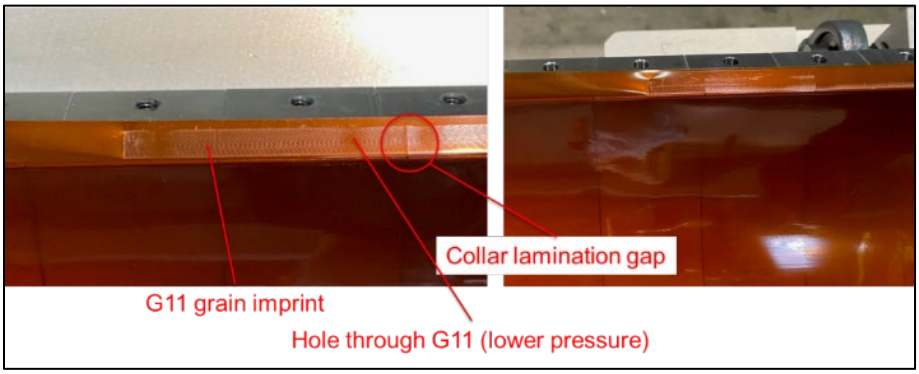

Figure 4.4: Imprints in the Kapton of Q3: collar lamination lines, G11 grain, and "lower pressure" spots at every hole in the G11 keys.

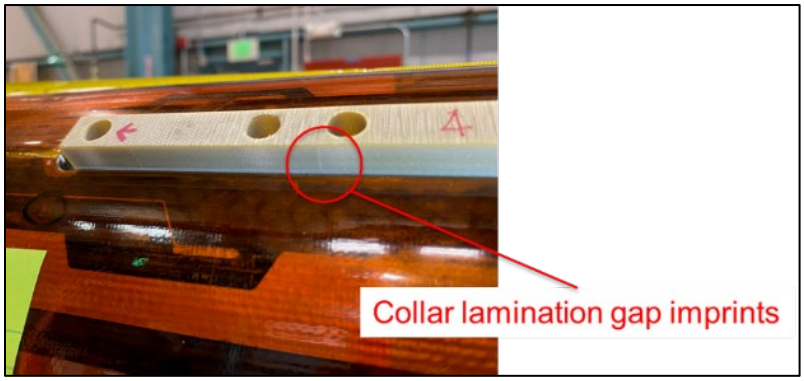

Figure 4.5: High pressure "imprints" of collar lamination gaps in the pole keys of Q3.

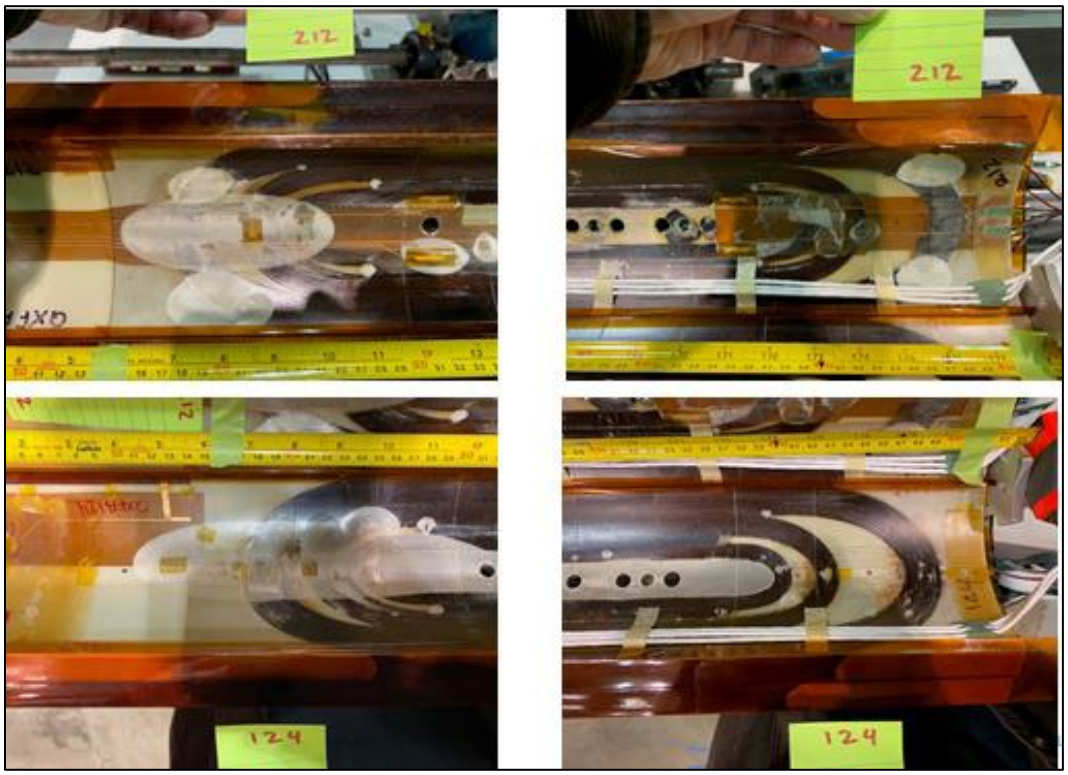

Figure 4.6: Inner surface of coil 212 and 124 in the end region after test.

Figure 4.7: Inner surface of coil 114 and 214 in the end region after test.

4.4. Axial rods

The MQXFA07 axial rod unloading process was supposed to be carried out in three steps:

- Step 1: From ~950 με to ~460 με (then half azimuthal unloading)
- Step 2: From ~460 με to ~50 με (then full azimuthal unloading)
- Step 3: From ~50 με to 0 με

However, it was observed that the nuts on rods 1, 2, and 4 all were loose after the 2nd step (Rod 3 remained snug). Therefore, a slight tension (increase of ~25 με) was added to these rods before proceeding to fully unload the azimuthal preload.

In addition, a residual strain in rods 1, 2, 4 of about ~200-300 με was measured at the end of the unloading. No residual strain was observed in Rod 3 (Fig. 4.8).

The rods length was not measured prior to the assembly, so a comparison was not possible with the length post-test. Relative lengths after disassembly appears to show that rods 1, 2, 4 each were ~1 mm longer than rod 3 (Fig. 4.9). However, some variations are expected from the unchamfered rolled threads ends. Therefore, these observations are inconclusive.

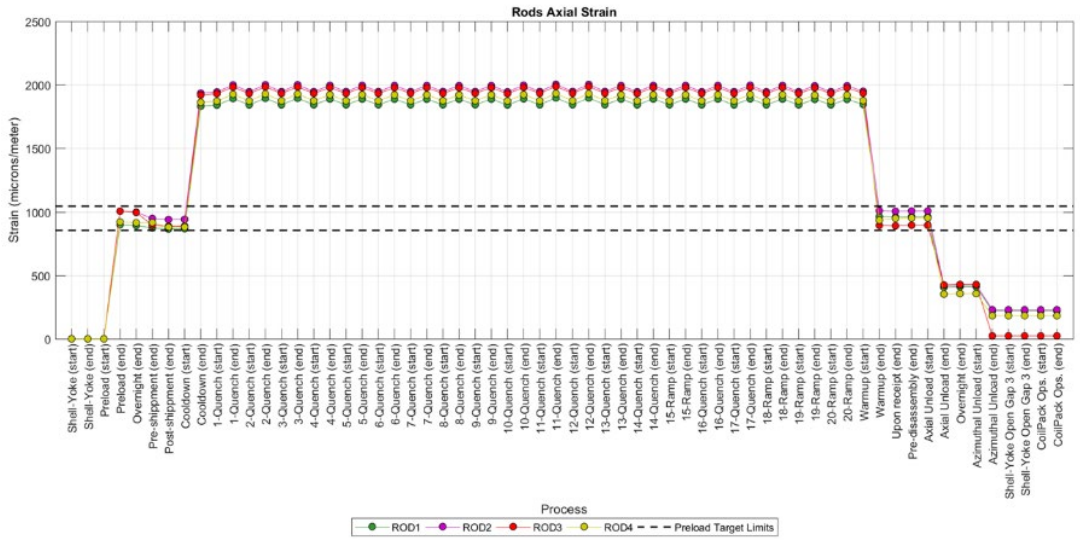

Figure 4.8: Rod axial strain history.

Figure 4.9: Rods after disassembly.

5. FE Analysis of closed Gaps

The effect of a closed pole key gap in quadrant 3 on the coil stress was studied with three different finite element models: a 360-degrees, full cross-section 2D model (see Fig. 5.1, left), a 360-degrees, full cross-section 3D model (see Fig. 5.1, center), and an octant 3D model (see Fig. 5.1, right). Both 3D simulations reproduce a MQXF short-model (MQXFS, with a 1.2 m magnetic length). The results of the three analyses are described in the following sub-sections.

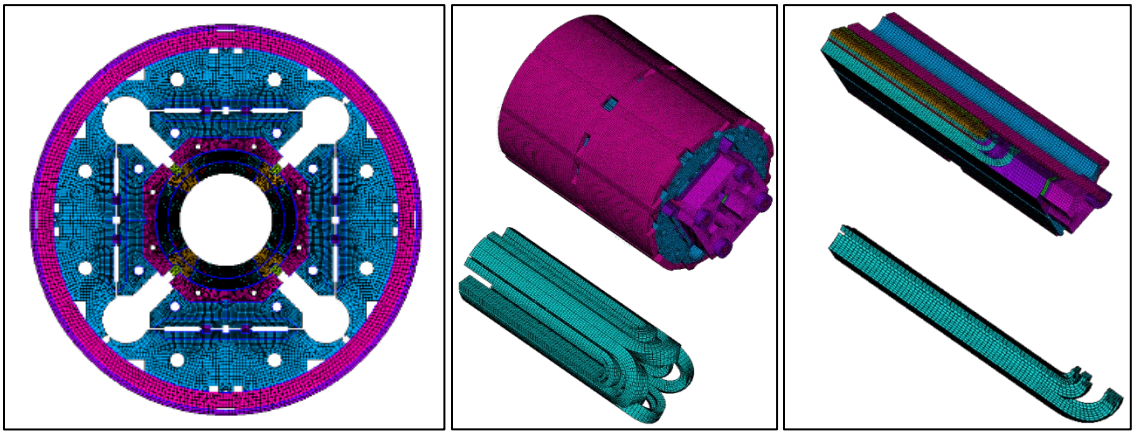

Figure 5.1: Left: 360-degrees, full cross-section 2D finite element model. Center: 360-degrees, full cross-section 3D model. Right: octant 3D model.

5.1. 2D finite element model (360-degrees, full cross-section)

According to the 2D model (which analyzes the magnet straight section), no 'special' stress singularity is observed in any of the quadrants. Nonetheless, the azimuthal pre-stress is significantly lower (~30 MPa reduction) in the quadrant with a closed pole-key gap (quadrant 3), 'medium' on the opposite side (quadrant 1), and maximum on the two remaining quadrants (see coil and shell computed stress in Fig. 5.2). It is important to point out that this reduction is not measured by the strain gauges mounted on the MQXFA07 coil in quadrant 3, in one axial location at 3.9 m from the lead end.

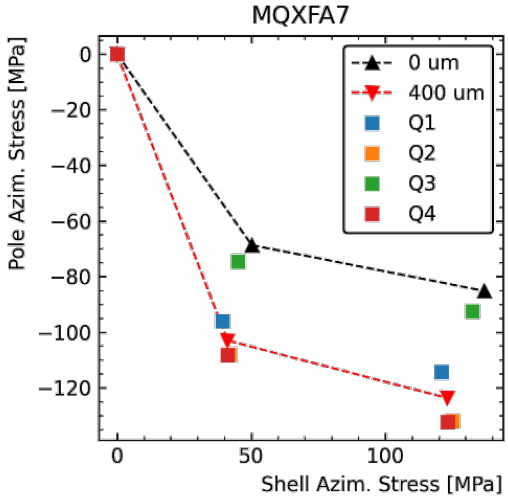

Figure 5.2: Coil pre-stress vs shell stress in the straight section assuming a closed pole key gap in quadrant 3.

5.2. 3D finite element model (360-degrees, full cross-section)

A 3D finite element model (360 degrees) confirms that the quadrant with the pole key gap closed has lower pre-stress than the quadrants with the open pole key gap, as can be seen in Fig. 5.3, where the coil azimuthal stress after cool-down computed by the 2D and 3D models (360 degrees) are compared.

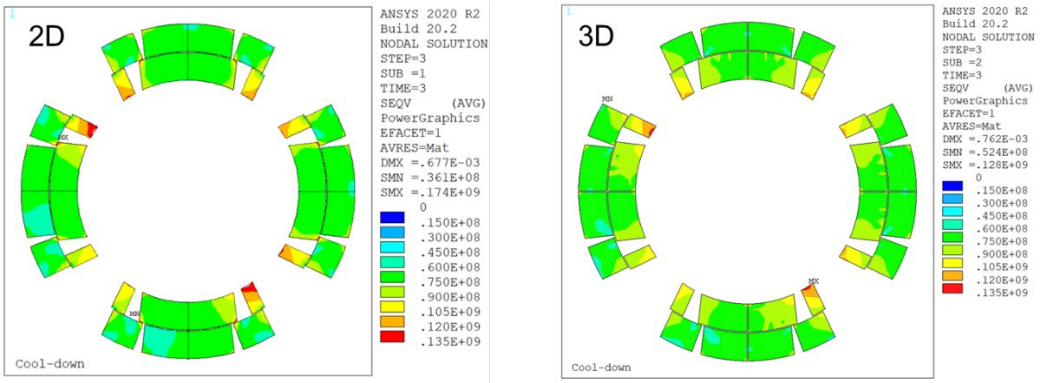

Figure 5.3: Comparison between coil azimuthal stress after cool-down computed by the 2D and 3D models (360 degrees).

In addition to the azimuthal stress in the straight section, the 3D model (360 degrees) allows to investigate the behavior of the four quadrants in the end region considering the MQXFA07 scenario. If we focus on the axial pre-load system, we notice that the computed stress is identical in the 4 rods (see Fig. 5.4, left): this indicates that the four rods have the same displacement. However, the axial force delivered by the end plate to the coil in quadrant 3 is smaller compared to the other quadrants (Fig. 5.4, right). This phenomenon can be explained as follows: the lower azimuthal pre-load in quadrant 3 results in a lower friction between the coil and the structure. Therefore, when compressed by the end plate, the quadrant 3 coil contracts axially more than the other coils, which are better axially constrained by the higher frictional contact with the support structure.

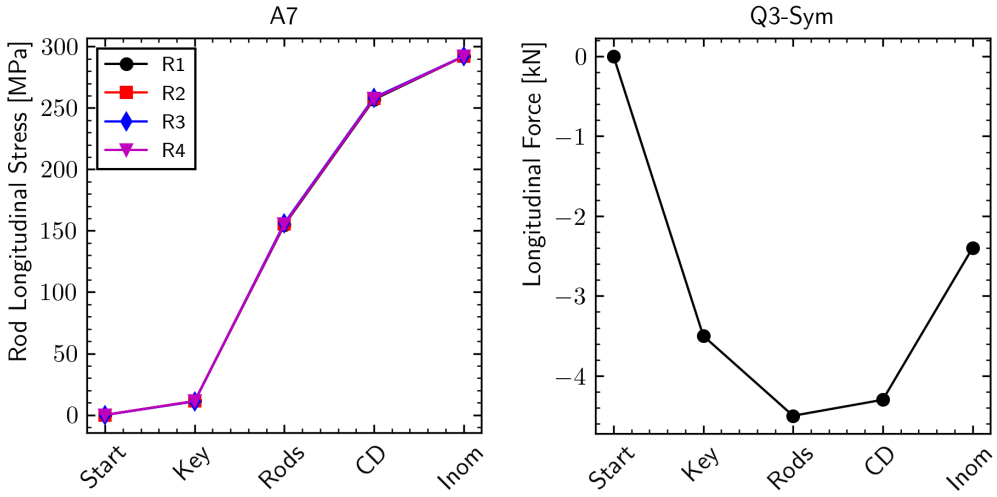

Figure 5.4: Left: axial rod stress in the MQXFA7 scenario. Right: difference between axial force delivered by the end-plate in quadrant 3 and in the other quadrants, in the MQXFA7 scenario.

If now we focus on the contact area between the wedge and the end spacer in layer 1, we see that, if we assume that all the coil surfaces are bonded, a tension occurs in quadrant 3 during excitation, as shown in Fig. 5.5. More precisely, when Lorentz forces are applied, the average tension between wedge and end-spacer is about 30 MPa in quadrant 3, while it remains close to zero in the other quadrants.

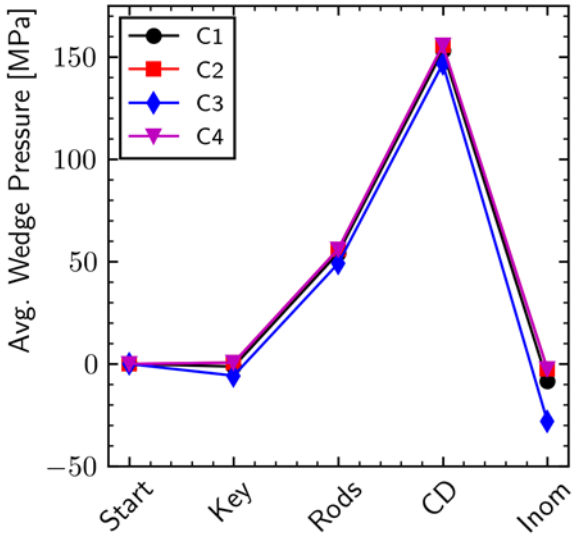

Figure 5.5: Average contact pressure (negative in tension) between wedge and end-spacer in the bonded case.

In summary, a higher tension between the spacer and end-shoe is observed in the Q3 due to the lower azimuthal and axial pre-load caused by the closed pole key gap. The higher tension results in a higher possibility of epoxy cracking between the wedge and the end-spacer.

5.3. 3D finite element model (octant)

The impact of a possible separation between the wedge and the end-spacer on the coil strain was studied with an octant model, which allows a more refined mesh compared to the 360 degrees model. Under the assumption that the coil surfaces are not bonded, i.e. that epoxy cracking has occurred, the gap between wedge and end-spacer, showed in Fig. 5.6 (left), increases with progressively lower azimuthal and axial pre-load, i.e. the conditions of Q3 in the MQXFA07 scenario according to the 360 degrees 3D model. The gap induces a spike in axial strain in the coil, which can reach the 0.4% level (see Fig. 5.7, left). As can be seen in Fig. 5.7, right, a larger increase is computed in the turn towards the pole.

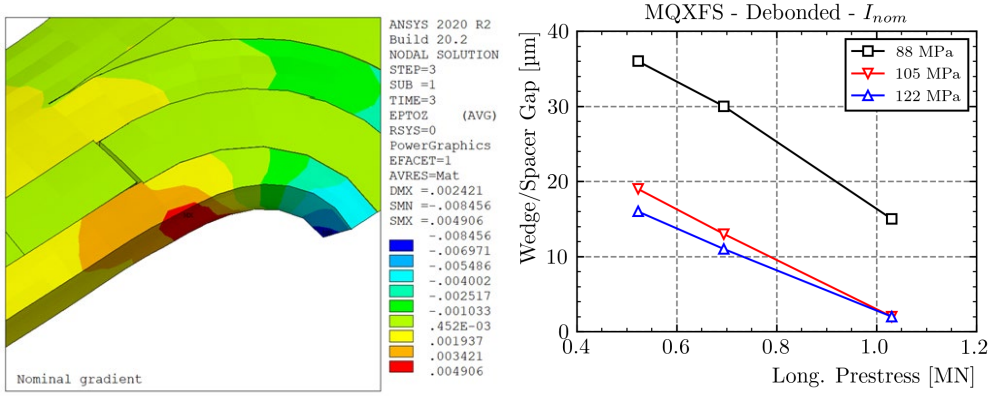

Figure 5.6: Left: View of the gap between wedge and end-spacer in the no-bonded case. Right: variation of the gap as a function of the azimuthal and axial pre-load.

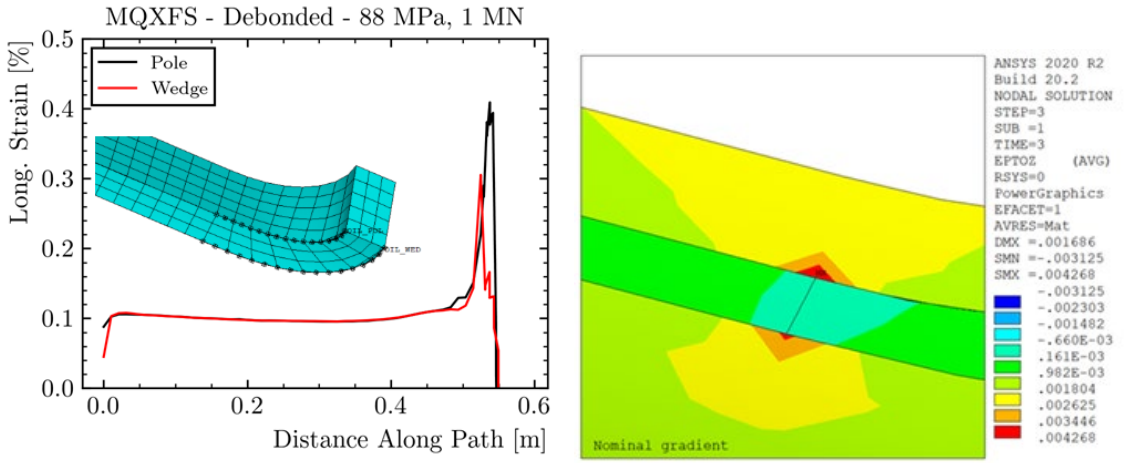

Figure 5.7: Left: Analysis of coil axial strain (pole block) in correspondence of the transition zone from end-spacer to wedge. Right: view of the increase in axial strain close to the gap in the pole block (top) and mid-plane block (bottom).

5.4. Conclusions of finite element analysis

The results of the finite element analysis carried out with both 2D and 3D models can be summarized as follow:

- A closed pole key gap in quadrant 3 determines both a lower azimuthal and axial pre-load with respect to the other quadrants.
- As a result, a higher tension develops in the wedge/end-spacer interface, with a higher risk of epoxy cracking.
- In the case of a de-bonded wedge/end-spacer interface, the resulting gap creates a peak of axial strain in the coil turns adjacent to the wedge.

6. Coil 214 Inspection and Autopsy

6.1. Coil 214 Visual Inspection

Coil 214 was inspected at LBNL after MQXFA07 disassembly. Lead and Return ends were cut according to the plan described in [10] and sent to FNAL for further visual inspection (Fig. 6.1). A report of inspection at LBNL is available at [11]. Subsequently, both ends were sent to CERN for CT-scan.

The visual inspection of coil 214 ends found:

- Both ends show large bubbles (delamination of the insulation on coil inner surface) on the inner layer at coil tips. These bubbles are typical in MQXF coils after test. Nonetheless, it is interesting to see that in coil 214 Lead End there is one large bubble, whereas in the Return End there are two smaller bubbles.
- Small bubbles are visible on coil inner surface where the voltage taps are connected to the short instrumentation traces and in random locations.
- A closer look at both ends shows that there is a small bubble/delamination at each transition between wedge and end-spacer (an example is visible in Fig 6.2).
- In addition, Figure 6.2 shows light scratches on coil inner surface starting from the wedge to end-spacer transitions in the Lead End.

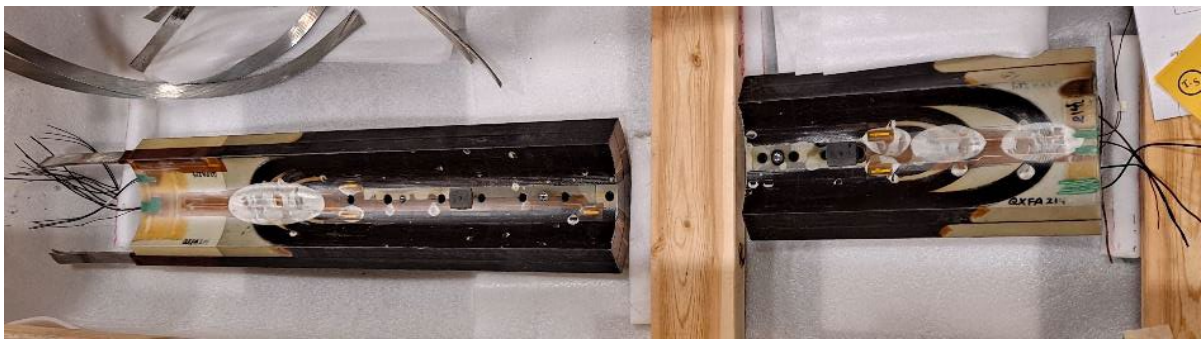

Figure 6.1: Coil 214 Lead (left) and Return (right) ends

Figure 6.2: detail of coil 214 Lead End. The yellow box shows the position of "scratches" starting from the wedge to end-spacer transition

6.2. Tomography of Coil 214 Lead End

At CERN Bartosz Bulat lead the CT-scanning, performed at Diondo GmbH (Germany) with a 6 MeV Linac [12], and did image reconstruction. A detailed presentation of the results can be found at [13]. Table

2 shows the number of popped strands found in both ends, taking into account that: *"As one popped in/out strand can induce a wave of events the numbers below show only the amount of conductors affected by the pop in/out effect. So even if there are more than one event in the same cable it is counted as one."*
An image of the CT scan through the Inner Layer of coil 214 Lead End is visible in Figure 6.3. The yellow boxes highlight the location of two popped strands.

Table 2: Number of popped strands in coil 214 ends

Coil 214 section	# in Outer Layer	# in Inner Layer inside A3-A4	# in Inner Layer outside A3-A4
Lead End	3	1	1
Return End	5	0	2

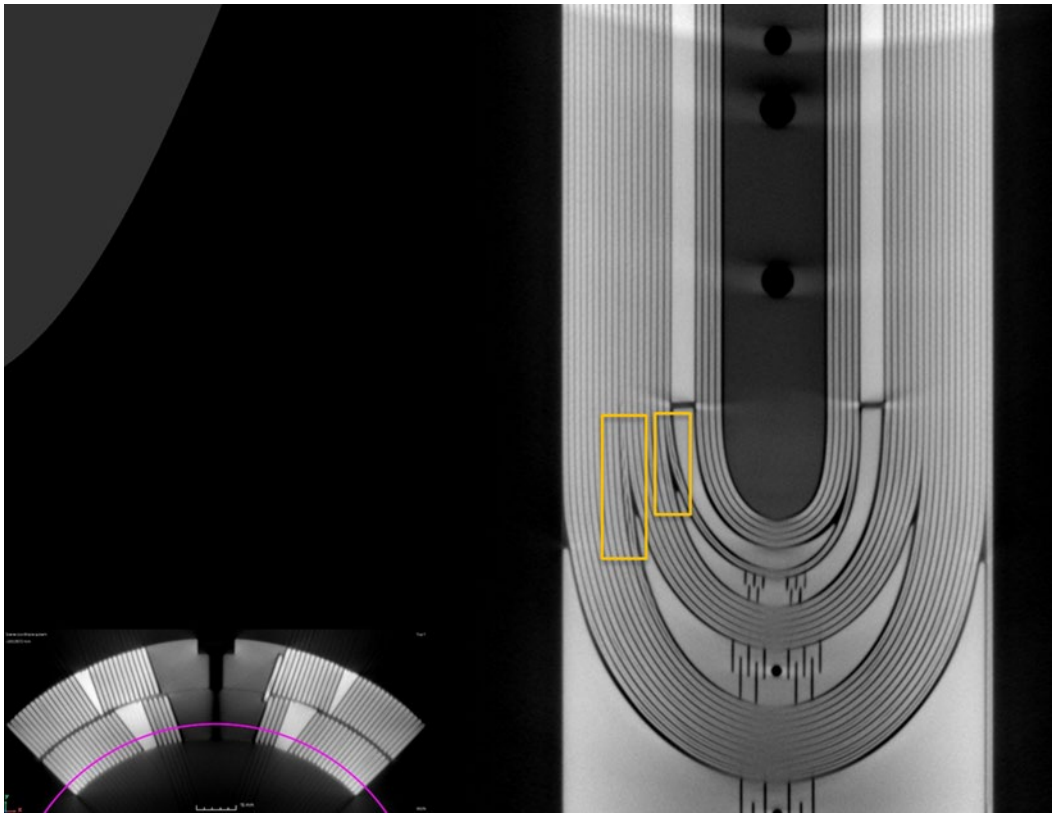

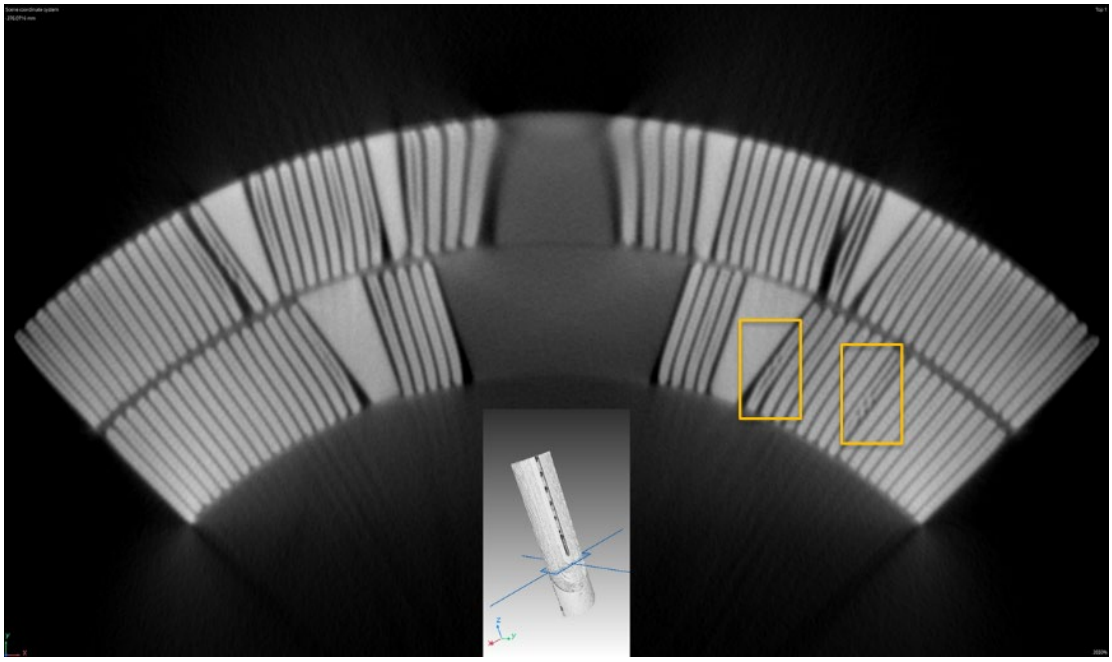

Figure 6.3 (Top): Image reconstruction of CT-scan through the Inner Layer of coil 214 Lead End. The purple line on coil cross-section shows the radial position. The yellow boxes highlight the location of two popped strands. The innermost one is within A3-A4 segment. (Bottom): Image reconstruction of coil radial cross-section at the location of the popped strands shown in the top picture.

6.3. Dye-penetrant test of Coil 214 Lead End

After the CT-scan dye-penetrant test was performed in order to check bonding among coil components. The large bubbles on coil ends were removed by cutting the delaminated insulation (Fig 6.4, left). The dye was applied to the inner radius surface of the coil (Fig 6.4, center) and the outer surface was subsequently examined for signs of paths through the coil (Fig. 6.4, right). Only two small paths were found on the Lead End (Fig 6.5).

After the go-through inspection, the dye penetrant was cleaned on the inner surface and revelator was applied on the same surface. Some cracks on the surface of the impregnated insulation layer were detected. These areas are signs of superficial cracks and can be seen in Figure 6.6. This test highlighted the surface cracks at the wedge to end-spacer transition (red ovals in Fig 6.6) identified during the visual inspection (Fig. 6.2).

More details can be found at [14]. The full set of images can be found at [15].

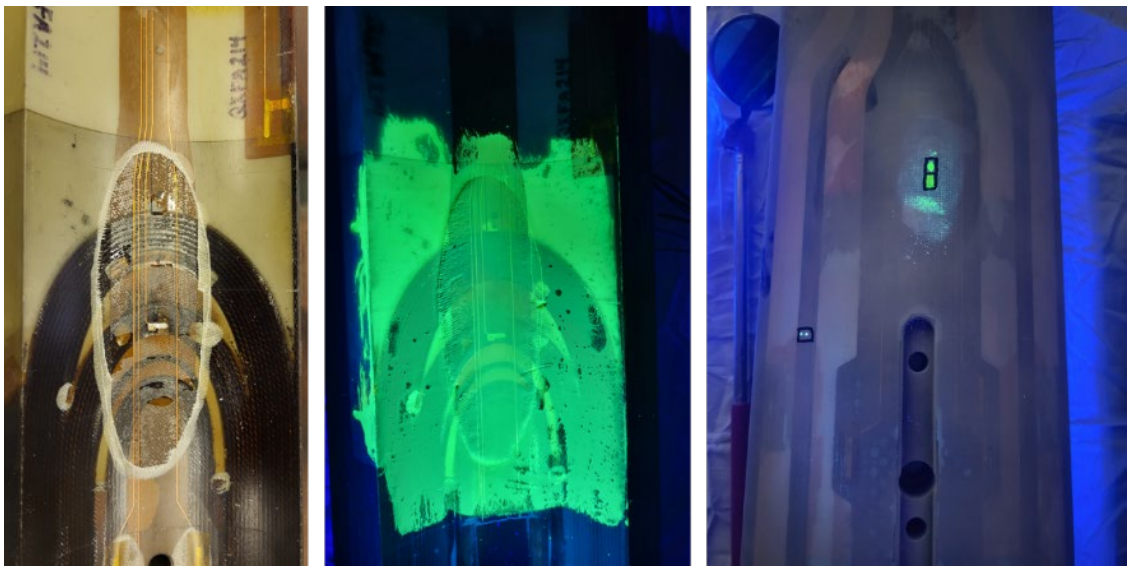

Figure 6.4: Procedure and results of dye penetrant test on coil 214 Lead End. The large bubble was removed by cutting the delaminated insulation (left); the dye was applied to the inner surface of the coil (center); the outer surface was subsequently examined for signs of paths through the coil (right).

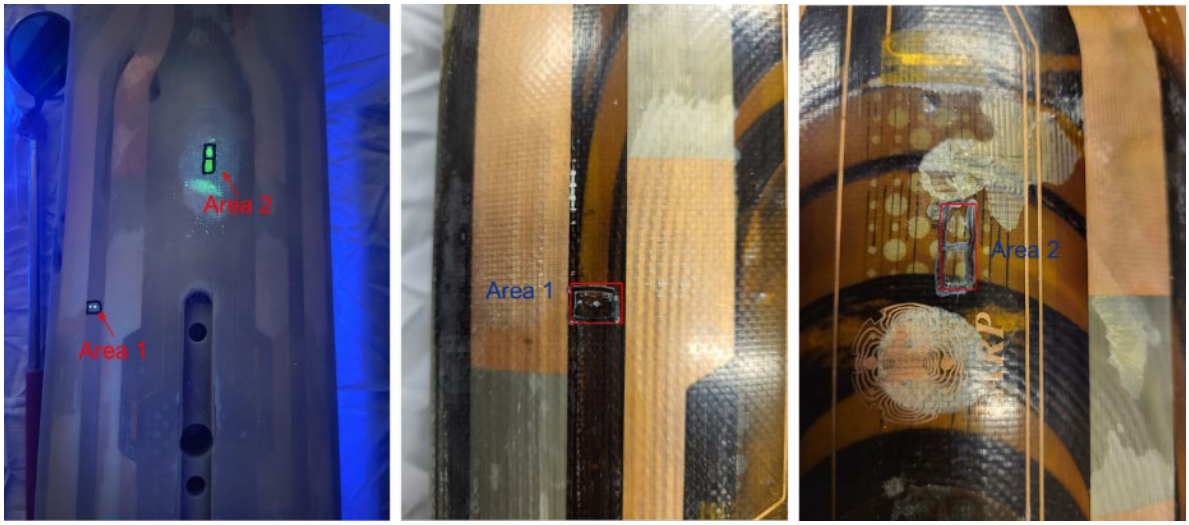

Figure 6.5: Areas were dye emerged on coil 214 outer surface in the Lead End

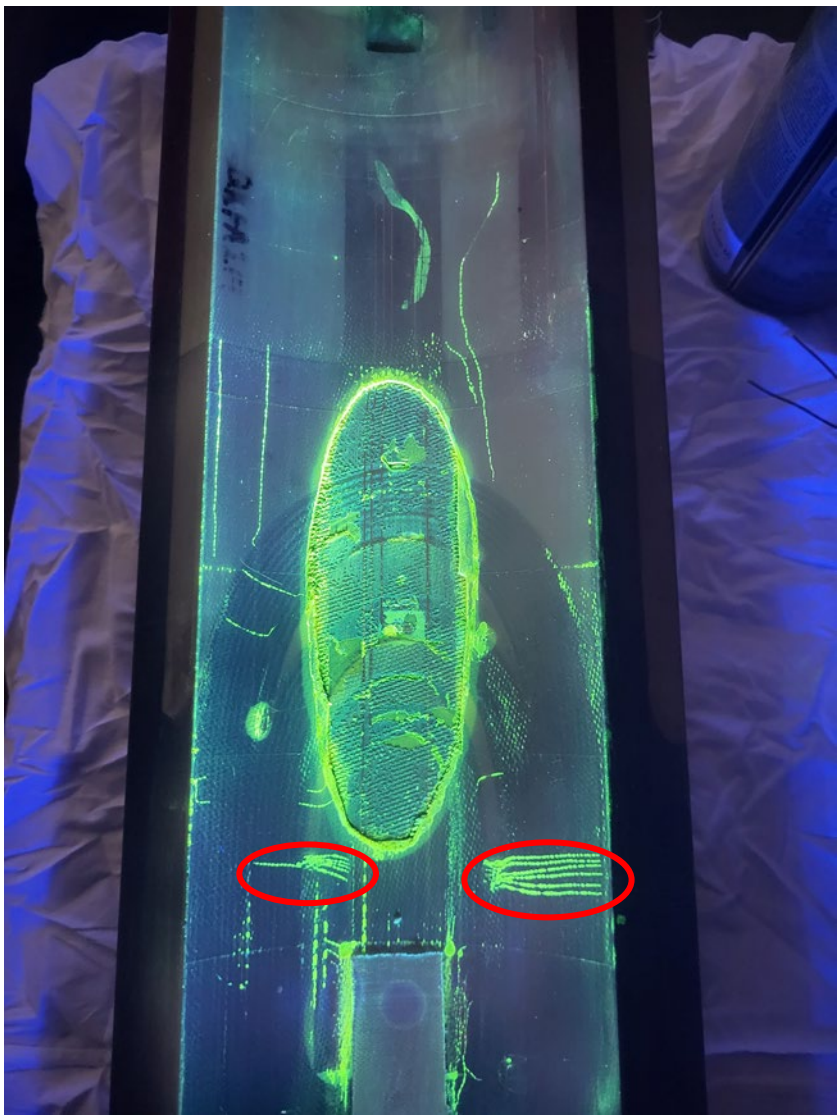

Figure 6.6: Inner surface of the Lead End showing some cracks on the surface of the epoxy-impregnated insulation layer. After the go-through inspection, the dye penetrant was cleaned on the inner surface and revelator was applied on the same surface to get this picture. The red ovals show the marks located/starting at the interface between wedges and end-spacers.

6.4. Micrographic Analysis of Coil 214 Lead End

Based on CT-scan results it was decided to perform macrographic analysis of 4 regions of the Inner Layer of coil 214 lead end. These regions are shown in Figure 6.7 and described below:

1. This is the wedge to end-part transition on both coil sides. The FE analysis described in section 5 has shown the possibility of strain concentration in this region due to the unusual elongation of coil 214 because of the closed gaps. Both visual inspection (Fig. 6.2) and die penetrant tests (fig. 6.6) showed signs of strain concentration in these regions. According to FE analysis, the cables most affected by this mechanism should be those on both side of each wedge to end-spacer transition.

2. This is the area where tomography showed a turn affected by popped strand(s) within the limiting segment (A3-A4). Micrographic analysis of this area is particularly challenging because the cable is not straight.
3. This is the area where the last collar lamination in contact with the pole-key ends. In case of sliding between this collar lamination and the next one (not supported by the pole-key) there could be a stress gradient in this region.
4. This is the tip of the end-spacer allowing turn 5 to move from the pole block to the mid-plane block. It is the other transition within the limiting segment (A3-A4). This sample was sent to Fermilab.

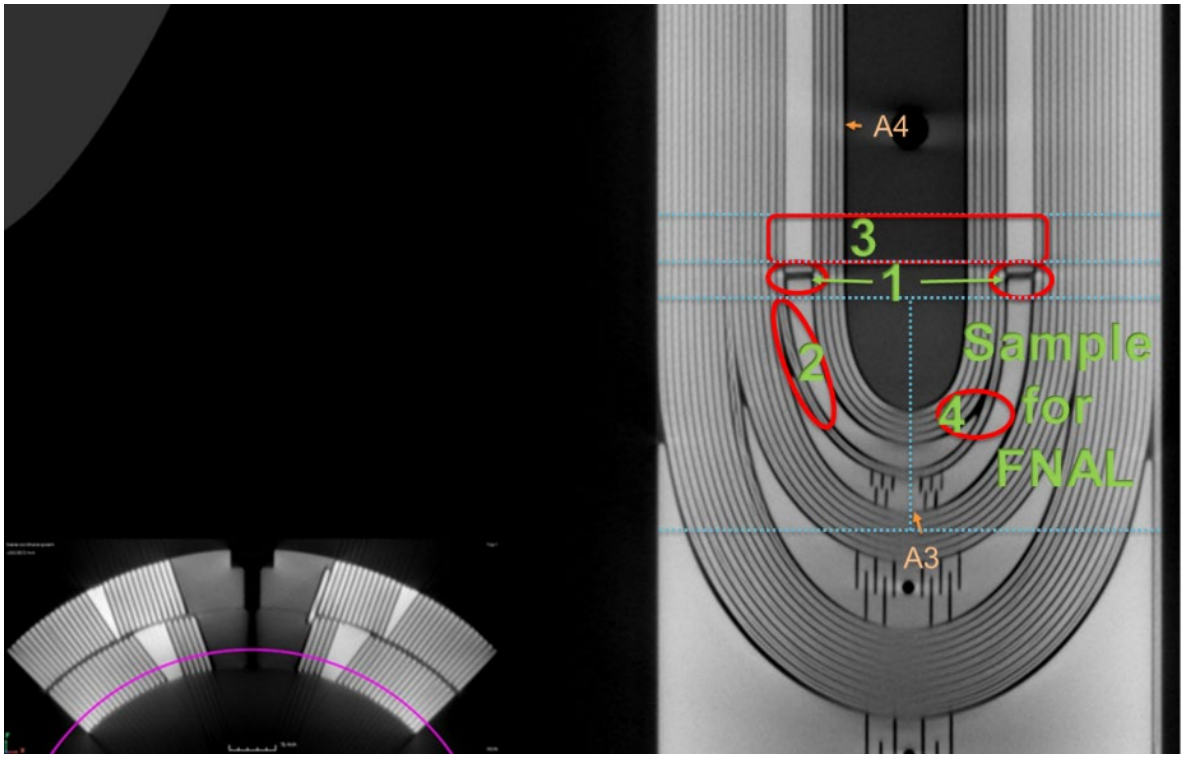

Figure 6.7. Areas in coil 214 Inner Layer Lead End selected for micrographic analysis.

The sample cut for micrographic analysis of area 1 is shown in Fig. 6.8. It is 10 mm thick and was ground and polished to approach the interface.

Micrographic analysis of this sample and inspection of superconducting filaments did not show any major event. Some radial "closed" microcracks were observed (Fig. 6.9) as in several other MQXF and Nb_3Sn-magnet cross-sections. These radial microcracks have been found to have no or very limited impact on current carrying capability: FIB-SEM analysis carried out at CERN shown that they are 20-30 µm deep, parallel with respect to the longitudinal axis of strand and not creating a total discontinuity through the SC phase that can still carry current. Other observations: 1) in addition to "usual" shrinkage cavities, some cracks through glass fibers/resin matrix were identified; 2) it was found that ceramic coating on end spacer ensures good cohesion with resin.

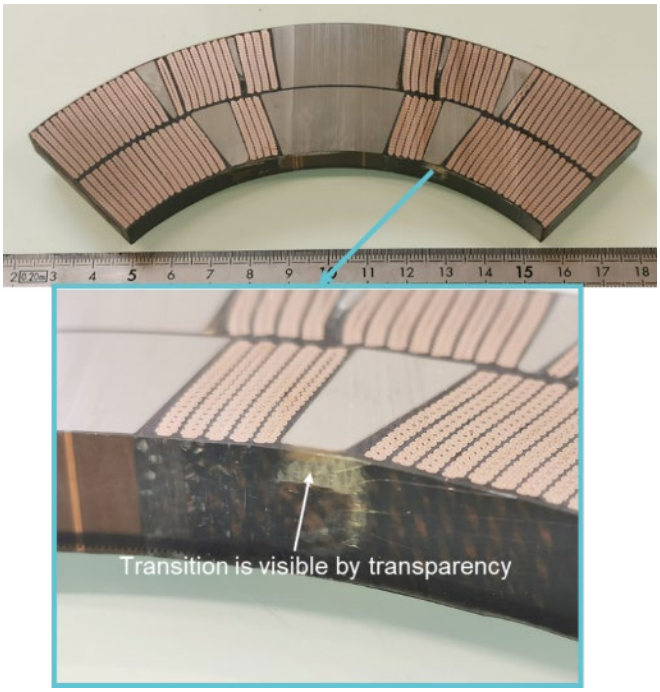

Figure 6.8. Sample for analysis of wedge to end-spacer transition

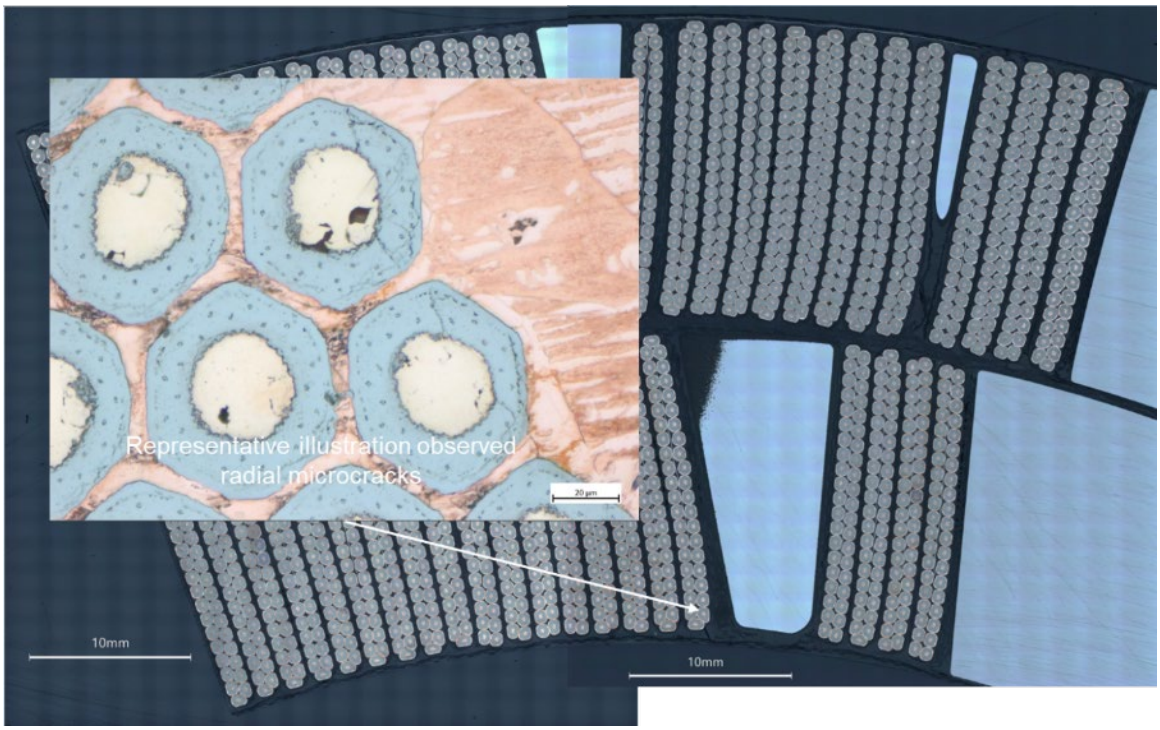

Figure 6.9. Example of radial microcracks.

The next step in the analysis of this sample was deep copper etching. Copper was dissolved with 50% HNO3 (according to ASTM E340) from 450 µm to 600 µm depth (layer jump side is shown in Fig. 6.10). The result is that not a single strand exhibited collapsed filaments.

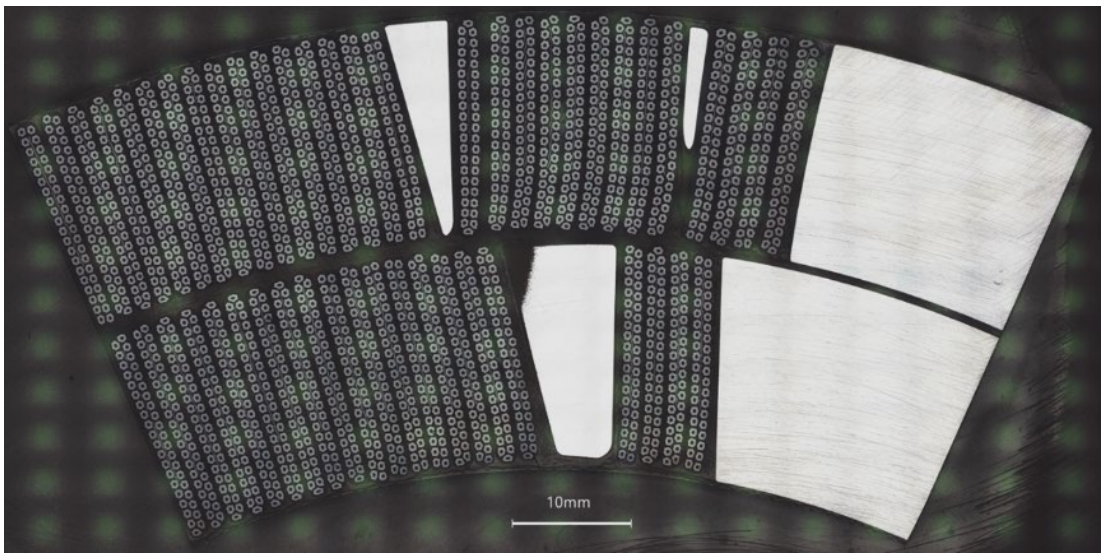

Figure 6.10. Layer jump side of sample 1 after copper etching. No strand exhibited collapsed filaments.

In order to assess strand integrity along the whole transition it was decided to extract smaller samples (yellow boxes in Fig 6.11) and to perform longitudinal cuts on the 2 cables facing the wedge to end-spacer transition on both coil sides (i.e. 4 cables total). The longitudinal cuts are to be performed along the cable side facing the transition (red lines in Fig. 6.11).

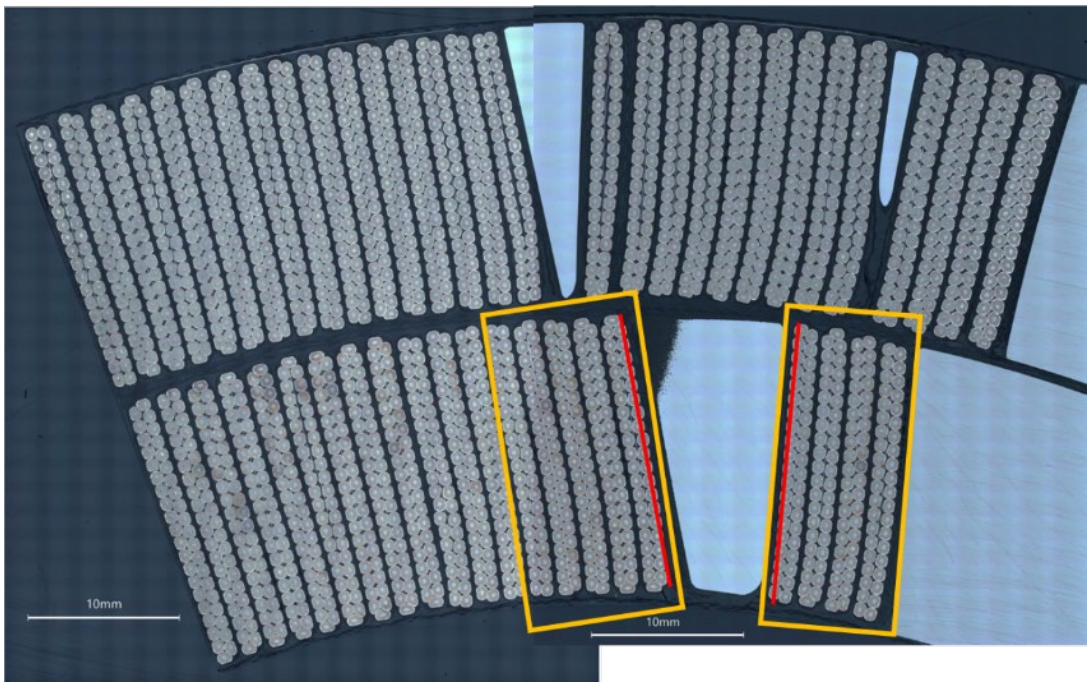

Figure 6.11. Plan for longitudinal cuts along wedge to end-spacer transitions

The results of the metallurgical inspection of area 1 are presented in Figure 6.12 - 6.14 and in Table 3. Figure 6.12 shows samples extracted from the layer-jump side, and Figure 6.14 shows samples from the non-layer-jump side. In these figures every red marker indicates a crack in a Nb_3Sn filament (sub-element). Figure 6.12 shows that on the layer-jump side many cracks were found on the cable included in the pole block, whereas no cracks were found in the cable included in the midplane block. Longitudinally, the cracks are concentrated in a narrow section (~ 2 mm wide), and they can be found in all strands on the side of the cable facing the wedge-spacer transition. Figure 6.12 shows a detailed image of some cracks. Figure 6.14 shows that on the non-layer jump side a few cracks (54) were found on the cable in the midplane block, whereas the cable in the pole block had 728 cracks.

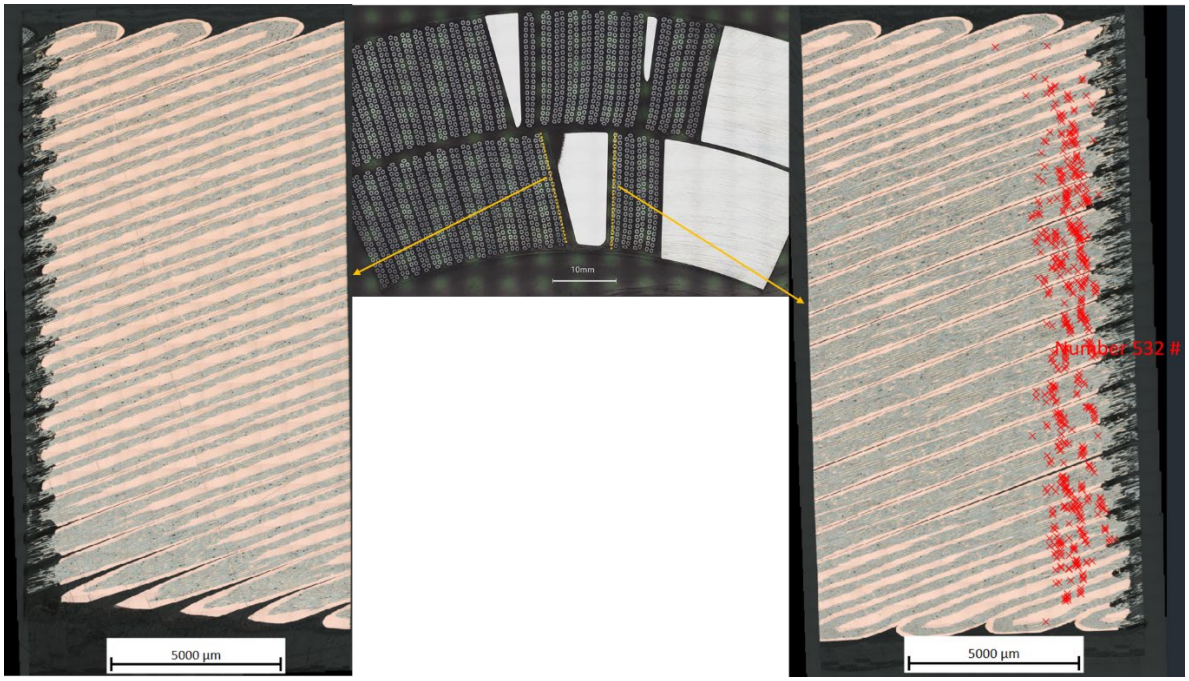

Figure 6.12. Metallurgical inspection of cables adjacent to the wedge-spacer transition in the Lead End layer-jump side of coil 214. Each red marker shows a cracked Nb_3Sn filament (sub-element).

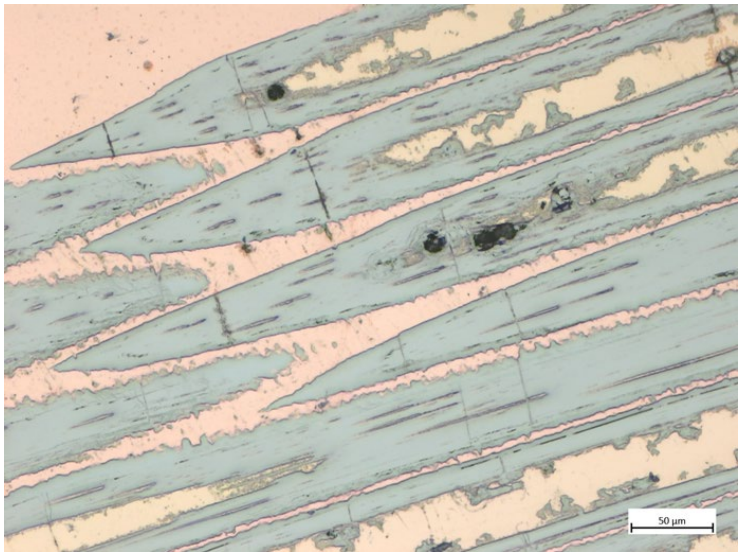

Figure 6.13. Example of some cracks shown in Fig. 6.12.

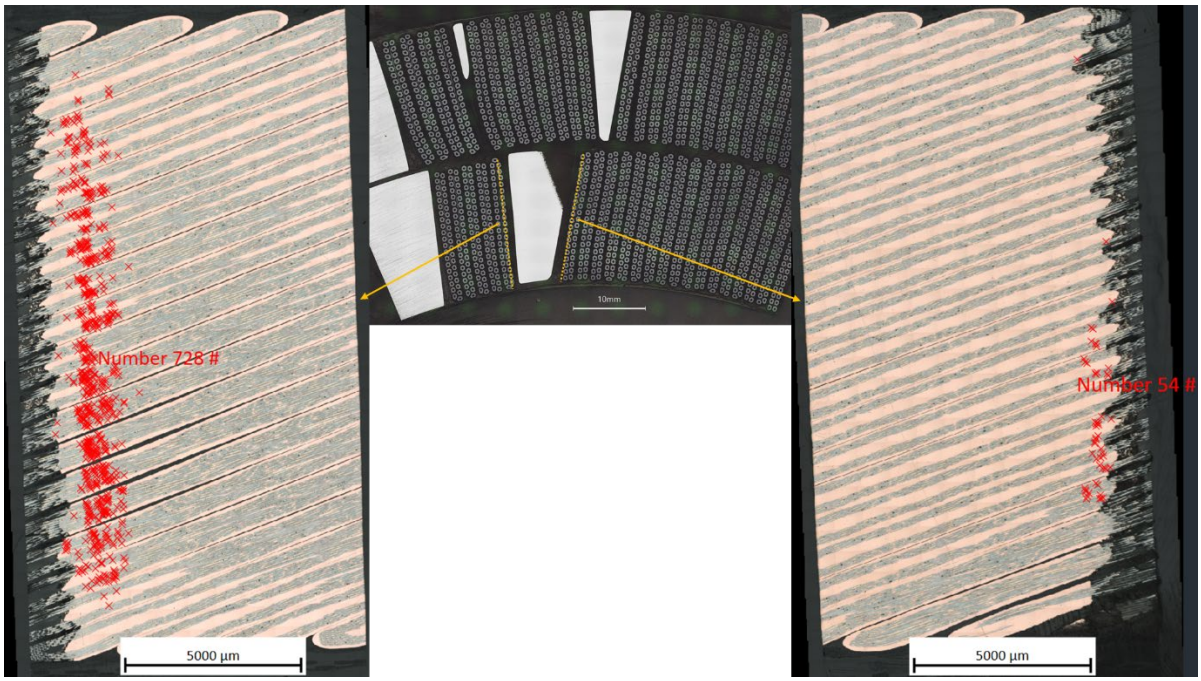

Figure 6.14 Metallurgical inspection of cables adjacent to the wedge-spacer transition in the Lead End non-layer-jump side of coil 214. Each red marker shows a cracked Nb_3Sn filament (sub-element).

In order to assess if there is damage also on the second layer of strands (i.e. on the cable side opposite to the wedge-spacer transition), the same metallurgical analysis was performed also on the second layer of strands in the cable with 728 broken filaments in Figure 6.14. Not a single cracked filament was found on that cable sample.

Table 3 presents a summary of this metallurgical inspection of samples extracted from coil 214 Lead End cables adjacent to the wedge-spacer (W-S) transitions. These results show that the strain field was concentered at the W-S transition, that the strain was significantly larger on pole-block side than on the midplane-block side, that is affected only some cables adjacent to the W-S transition, and that it did not propagate to the second layer of strands (i.e. those further from the W-S transition).

Table 3: Summary of metallurgical analysis of samples close to the Wedge-Spacer (W-S) transition from coil 214 Lead End

#	Samples adjacent to W-S transition from coil 214 Lead End	Number of cracked filaments
1	Layer-jump side, cable in midplane block, side adjacent to W-S transition	0
2	Layer-jump side, cable in **pole block**, **side adjacent to W-S transition**	**532**
3	Non-layer-jump side, cable in midplane block, side adjacent to W-S transition	54
4	Non-layer-jump side, cable in **pole block**, **side adjacent to W-S transition**	**728**
5	Same cable of sample 4, side opposite to the W-S transition	0

The detailed position of the cracks with respect to the wedge-spacer transition is shown in Figures 6.15 and 6.16. Figure 6.15 shows the color scheme used to show the position of filament cracks with respect to the W-S transition in Figure 6.16: A (light blue): End spacer + ceramic coating ≈ 0,5 mm; B (grey): resin (filled with S-2 glass) between end spacer and wedge ≈ 1,5 mm; C (light yellow): copper wedge.

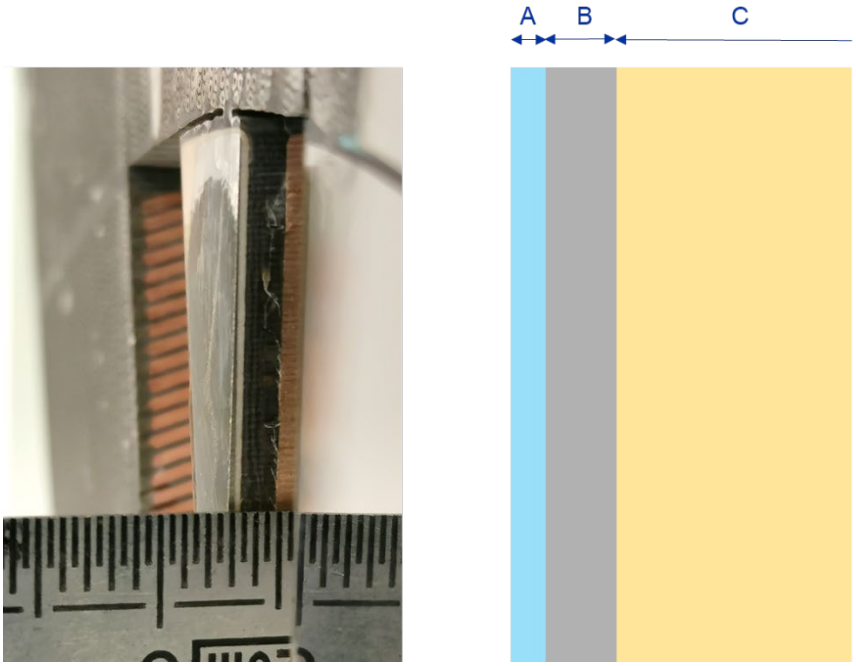

Figure 6.15. Left: coil section shown in Fig. 6.8 after samples were extracted for metallographic inspection. Right: color scheme used to show the position of filament cracks with respect to the W-S transition in the following figure. A: End spacer + ceramic coating ≈ 0,5 mm; B: resin (filled with S-2 glass) between end spacer and wedge ≈ 1,5 mm; C: copper wedge.

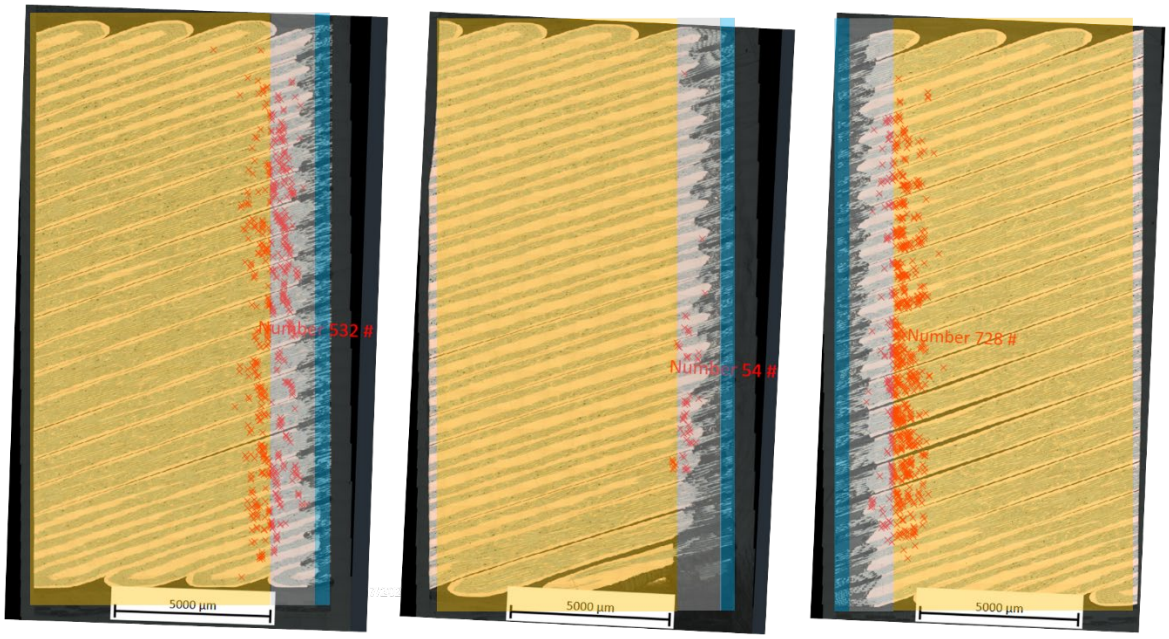

Figure 6. 16. Position of filament cracks with respect to the W-S transition. The color scheme is described in the previous figure. Filament cracks are clearly clustered around the transition between the wedge and the resin (filled with S-2 glass).

Figure 6.16 shows that filament cracks are clearly clustered around the transition between the wedge and the resin (filled with S-2 glass). This is consistent with the observation made above that “ceramic coating

on end spacer ensures good cohesion with resin" and that the bonding between the copper wedge and the resin is not as strong.

7. Conclusions

The data and analyses presented in this report have shown that:

- MQXFA07 was limited by self-field instability enhanced by conductor damage.
- All limiting quenches started in coil 214 inner layer Lead End (close to the pole tip) in the multi-turn block including turns 2 to 6.
- During winding of coil 214 a strand popped out twice in the inner layer Lead End at the transition between turn 5 and 6.
- The fabrication of coil 214 was interrupted during the Covid lockdown after winding and curing of the inner layer. For about 14 weeks, it remained on the winding mandrel, with inner layer pushers bolted in place supporting midplane, numerous Velcro straps securing coil OD and coil ends, and covered in plastic.
- During MQXFA07 dis-assembly it was found that all pole-key gaps of coil 214 (in quadrant 3) were closed, whereas all other gaps of all other coils were open.
- Changes to the magnet assembly procedures due to Covid requirements are understood to have increased the probability of small pole-key gaps in a magnet quadrant.
- Finite element analysis found that MQXFA07 pole-key gap asymmetry reduced the axial pre-load on coil 214 allowing tension at the wedge-spacer transition in coil ends during magnet powering.
- After MQXFA07 disassembly, coil 214 inspection (visual and die-penetrant tests) showed signs of tensile strain at the wedge-spacer transitions in the inner layer of the lead end.
- CT-scan of coil 214 ends showed a popped strand in the inner layer of the lead end at the transition turn 5 and 6. It is on the layer-jump side, whereas the popped strand recorded during winding was on the non-layer-jump side (at about 4 cm distance on same turn).
- Metallographic inspection of the cables adjacent to the wedge-spacer (W-S) transitions in the inner layer of the lead end showed large number of cracked Nb_3Sn filaments. Most cracks (500-700 per cable) are found in the cables of the pole block. All cracks are on the cable side facing the W-S transition, whereas no cracks are visible on the other side of the same cable. This is consistent with the strain concentration found in FE analysis.

Based on these findings, we understand that coil 214 pole-key gaps were closed at cold, whereas those of other coils were open. During magnet energization this difference caused high tensile strain at wedge-spacer interfaces in coil 214 ends. In early ramps to quench (possibly before or during ramp #4) the bonding between the copper wedge and the resin (filled with S-e glass) gave away in the lead end increasing the strain on the strands closest to that interface. The "increased" strain degraded some strands and triggered the enhanced self-field instability behavior. This mechanism caused quench #4 and all subsequent quenches at 1.9 K and 20 A/s. These quenches, with hot-spot close to the wedge-spacer interface, may have exacerbated the degradation mechanism by increasing local strain and strand damage, and therefore causing the current drop (~1 kA) from quench #4 to #8.

8. References

1. MQXFA07 Fabrication report, US-HiLumi-doc-4197
2. Acceptance Criteria Part A: MQXFA Magnet, US-HiLumi-doc-1103 and CERN EDMS# 2031083
3. MQXFA07 Test Results Meeting, Nov. 4, 2021, https://indico.fnal.gov/event/51196/
4. G. Ambrosio et al., "Progress in the Long Nb3Sn Quadrupole R&D by LARP", IEEE Trans. Appl, Superc. Vol 22, # 4003804 (2012).
5. H. Bajas et al., "Test Results of the Short Models MQXFS3 and MQXFS5 for the HL-LHC Upgrade", IEEE Trans. Appl. Superc. Vol 28, # 4007006 (2018).
6. B. Bordini, et al., IEEE Trans. Appl. Superc., vol. 22, 2012, # 4705804
7. A. K. Ghosh, IEEE Trans. Appl. Superc., vol. 23, 2013, # 7100407
8. Analysis of MQXFA08 Test Non-Conformity, in progress
9. MQXFA07 and MQXFA08 Quality Investigation Report, US-HiLumi-doc-4266.
10. MQXFA07 Inspection Plan, US-HiLumi-doc-4222.
11. MQXFA07 Visual Inspection after Disassembly, US-HiLumi-doc-4273.
12. Linearbeschleuniger CT System zur Analyse und Prüfung (diondo.com)
13. Coil 214 tomography at "CERN-AUP Coil WG on coil 108 metallography, coil 214 tomography and next steps": https://indico.cern.ch/event/1147468/
14. Dye penetrant test on coil 214 at "Coil WG mtg" on May 5, 2022: https://indico.fnal.gov/event/54388/
15. CERN EDMS # 2734961 – may require authorization

9. Appendix

9.1. Measurement of MQXFA strand stability

Christian Barth, Marina Malabaila, Anne Eychenne, Florian Girardot, Pierre-Francois Jacquot, Ion Savu, Christian Szyma, Simone Morisi

Measurements of MQXFA strand stability were performed at CERN by Christian Barth & the team of building 163. Measurements were done on both virgin and extracted strands. Eight samples were measured at 1.9 K and 4.3 K, in background field from 15 T down to 6 T. Table 9.1 lists the samples tested. Six samples were extracted from the left-over sections of the cables used for coil 214 (limiting coil in MQXFA07) and coil 213 (limiting coil in MQXFA08). Two samples were round/virgin samples from two spools of extracted strands.

The figures below show measurement results. No sample showed sign of stability issued up to 2 kA.

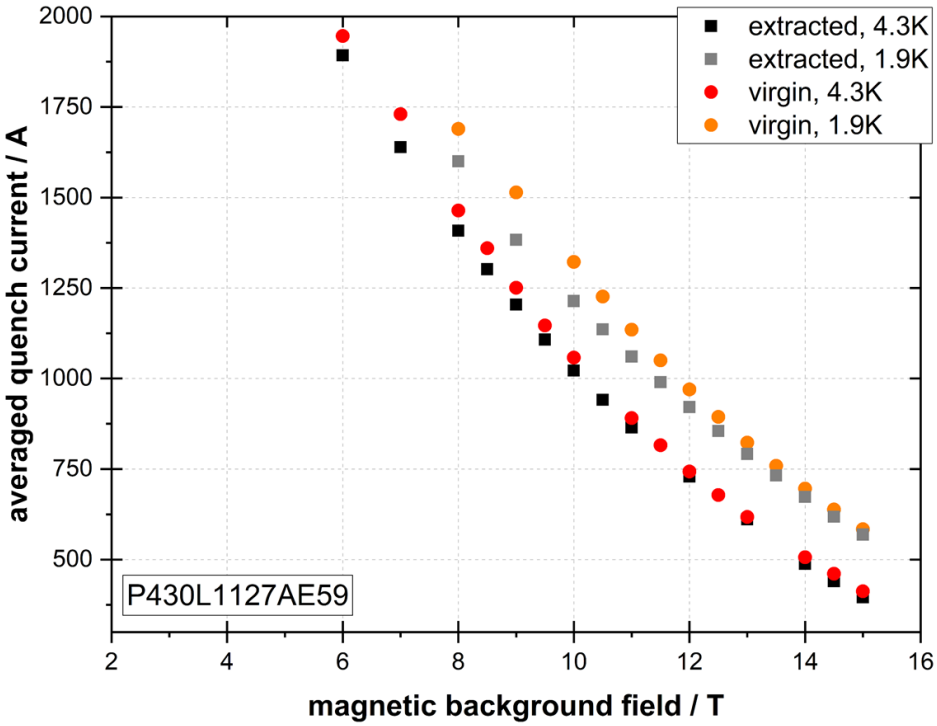

Figure 9.1. Samples: P430L1127AE59 extracted & virgin

Table 9.1: Samples used for MQXFA stability measurements

Magnet	Coil	Cable	Wire	Extracted Strand	Round Wire	Fork #	Strand #
MQXFA07	214	P43OL1127	PO08S00380A03U	**P43OL1127AE31E**		31	21
MQXFA07	214	P43OL1127	PO08S00365A02U	**P43OL1127AE57E**		57	38
MQXFA07	214	P43OL1127	PO08S00365A02U	**P43OL1127AE59E**	**P43OL1127AE59V**	59	39
MQXFA08	213	P43OL1123	PO08S00343A01U	**P43OL1123AE25E**		25	17
MQXFA08	213	P43OL1123	PO08S00343A01U	**P43OL1123AE27E**	**P43OL1123AE27V**	27	18
MQXFA08	213	P43OL1123	PO08S00363A01U	**P43OL1123AE43E**		43	29

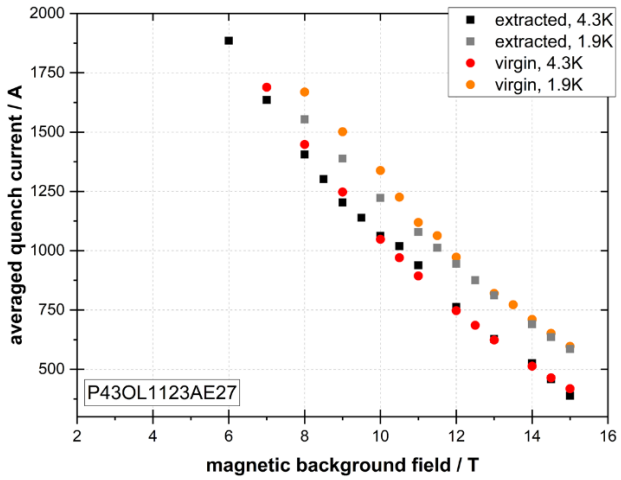

Figure 9.2. Samples: P43OL1123AE27 extracted & virgin

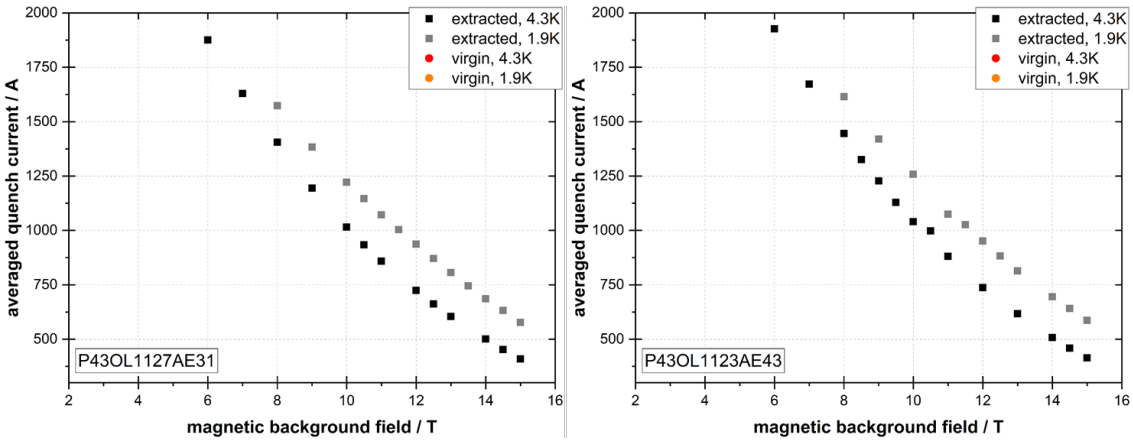

Figure 9.3. Samples: P43OL1127AE31 extracted (left) & P43OL1123AE43 extracted (right)

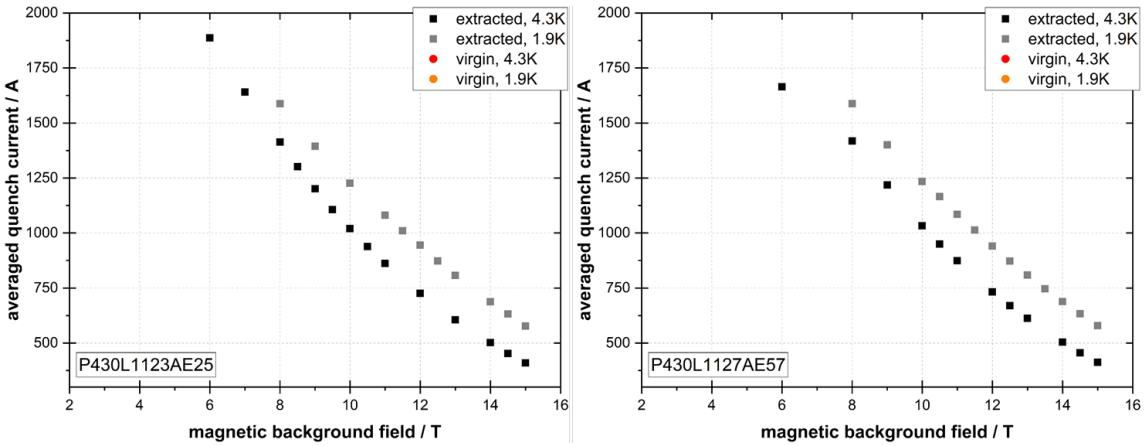

Figure 9.4. Samples: P430L1123AE25 extracted (left) & P430L1127AE57 extracted (rights)

9.2. Discrepancies regarding collapsed/roped cable in coils successfully tested in Pre-Series magnets

The first event reported in DR AM-164 is not very unusual, and several similar instances occurred during the fabrication of coils used in Pre-Series magnets MQXFA03, MQXFA04 and MQXFA06, which met requirements during vertical test at BNL. In the following we present these discrepancies in magnet chronological order.

Coil 202 used in MQXFA03:

DR AM-097: During winding the cable collapsed when winding around the coil end. It collapsed as the turn around the end was nearly complete. Issue occurred:

- Inner Layer, Turn 4, Return End
- Inner Layer, Turn 6, Return End
- Inner Layer, Turn 8, Lead End.

DR AM-100: During winding the cable collapsed as it was paying out while winding in the straight section of the coil. Issue occurred:

- Outer Layer, Turn 15, straight section transition side
- Outer Layer, Turn 19, straight section transition side.

DR AM-101: During winding the cable collapsed when winding around the coil end. It collapsed as the turn around the end was nearly complete. Issue occurred:

- Outer Layer, Turn 1, Lead End
- Outer Layer, Turn 9, Lead End
- Outer Layer, Turn 9, Return End
- Outer Layer, Turn 10, Return End.

Coil 206 used in MQXFA04:

DR AM-124: Conductor wires began to tube; popping wires from the cable matrix. This occurred while winding around the lead end.

- Inner Layer, Turn 6, Lead End.

DR AM-125: Conductor wires began to tube; popping wires from the cable matrix. This occurred while winding around the non-lead end.

- Outer Layer, Turn 19, Return End

Coil 123 used in MQXFA06:

DR 11976: While making the first turn on the LE pole, the cable on the spool fell onto itself and got caught on itself. I lifted the cable to get it untangled, after the cable came off the spool it had roped. Cause of Discrepancy: There are 8 turns of cable per layer on the spool. When install the L2 cable spool on the tensioner, under no tension or low tension, the payout turn slid down and laid on top of the next turn of cable, causing cable rope during winding with higher tension.

- Outer Layer, Turn 1, Lead End, while cable was on spool.

Figure 9.5 and 9.6 show coil-123 cable before and after it was fixed.

Figure 9.5: Coil 123 roped cable after insulation was removed, and before cable was fixed

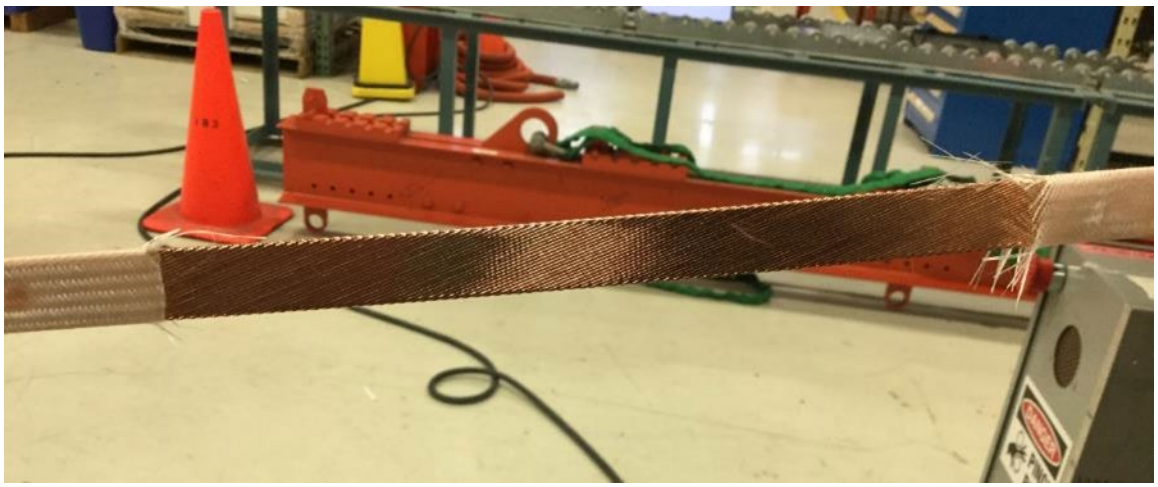

Figure 9.6: Coil 123 cable after it was fixed, and before insulation was replaced.